

# On the choice of viscous discontinuous Galerkin discretization for entropy correction artificial viscosity methods

Samuel Van Fleet<sup>a</sup>, Jesse Chan<sup>b,c</sup>

<sup>a</sup>*Department of Computational Applied Mathematics and Operations Research, Rice University*

<sup>b</sup>*Oden Institute for Computational Engineering and Sciences, The University of Texas-Austin*

<sup>c</sup>*Department of Aerospace Engineering & Engineering Mechanics, The University of Texas-Austin*

---

## Abstract

Entropy correction artificial viscosity (ECAV) is an approach for enforcing a semi-discrete entropy inequality through an entropy dissipative correction term. The resulting method can be implemented as an artificial viscosity with an extremely small viscosity coefficient. In this work, we analyze ECAV when the artificial viscosity is discretized using a local discontinuous Galerkin (LDG) method. We prove an  $O(h)$  upper bound on the ECAV coefficient, indicating that ECAV does not result in a restrictive time-step condition. We additionally show that ECAV is contact preserving, and compare ECAV to traditional shock capturing artificial viscosity methods.

---

## 1. Introduction

High order discontinuous Galerkin (DG) methods are often used to approximate solutions to time-dependent nonlinear conservation laws. High order approximations are efficient and accurate due to their small dissipation and dispersion error relative to low order methods. However, in the presence of under-resolved solutions such as shocks, high order methods can become unstable.

Artificial viscosity is another popular technique for stabilization; an incomplete list of examples is [8, 36, 38, 39, 49, 47, 50, 55, 70] and the references therein. Many artificial viscosity approaches utilize shock capturing to detect regions where the solution is under-resolved and add artificial viscosity to suppress Gibbs-type oscillations. One drawback is that these methods often rely on parameters that need to be tuned for different problems.

Entropy stable DG formulations were introduced in [11, 19, 34] to stabilize DG schemes without introducing heuristic stabilization parameters. The resulting methods are nodal DG formulations which use collocated Gauss-Lobatto quadrature nodes, resulting in mass and stiffness matrices which satisfy the summation by parts properties [33]. In addition, these methods rely on a “flux differencing” framework, which reformulates a standard nodal DG method to resemble an algebraic finite volume formulation with central fluxes. To enforce entropy stability, these central fluxes are replaced with entropy conservative finite volume fluxes [18, 42, 58, 66]. If a consistent two-point entropy stable numerical flux is used at the interfaces, the method satisfies a semi-discrete cell entropy inequality. These entropy stabilization techniques have also been extended to non-collocation formulations [13, 22].

---

*Email addresses:* [sv73@rice.edu](mailto:sv73@rice.edu) (Samuel Van Fleet), [jesse.chan@oden.utexas.edu](mailto:jesse.chan@oden.utexas.edu) (Jesse Chan)

Flux differencing entropy stable DG formulations have been successfully applied to several challenging problems involving the compressible Navier-Stokes equations in [53], Magnetohydrodynamics (MHD) equations in [9, 61], the shallow water equations [72, 73], and hypersonics [52, 56]. However, they require the computation of an entropy conservative numerical flux, which can be expensive to evaluate and complex to derive. Moreover, while the extension of such methods to more general discretizations is possible [13, 22, 46], the resulting entropy stable flux differencing formulation becomes more complicated.

Recently, entropy correction artificial viscosity (ECAV) methods were introduced in [14, 20, 21] as a simpler way of enforcing a cell entropy inequality. ECAV is closely related to the entropy correction terms from [1, 2, 28, 32, 51]. In [14] artificial viscosity determined based on the local violation of a cell entropy inequality. The artificial viscosity coefficients are locally computed over each element without parameters and were shown to be small for a number numerical examples involving the compressible Euler equations. The method is high-order accurate, satisfies the global semi-discrete entropy inequality, and has a large maximum stable time-step size when used in conjunction with explicit-time stepping schemes.

In this paper, we analyze the ECAV method from [14], which uses a BR-1 type scheme to discretize the artificial viscosity term. BR-1 discretizations of a Laplacian result in spurious non-constant null space eigenmodes [40, 62] which result in arbitrarily large artificial viscosity coefficients. We show that when the artificial viscosity term is discretized using a local discontinuous Galerkin (LDG) formulation [23, 25], it is bounded from above by  $O(h)$ . The resulting ECAV method results in smaller magnitude artificial viscosity coefficients and preserves the less restrictive hyperbolic CFL condition.

The organization of this paper is as follows: Section 2 reviews nonlinear conservation laws and different forms of an entropy inequality, Section 3 reviews a standard DG weak formulation for nonlinear conservation laws, as well as the LDG discretization of the entropy correction artificial viscosity term. In Section 4, we derive upper bounds on the artificial viscosity coefficients under LDG. In Section 5 we present numeral experiments that validate the robustness, high-order accuracy, entropy stability, and upper bounds of the artificial coefficients of the method. We compare the ECAV method with BR-1 [14] and LDG viscous discretizations, as well as with heuristic shock capturing approaches from [39, 55, 69].

## 2. Nonlinear conservation laws and entropy inequalities

In this paper, we focus on the numerical approximation of solutions to systems of nonlinear conservation laws in  $d$  spatial dimensions:

$$\frac{\partial \mathbf{u}}{\partial t} + \sum_{m=1}^d \frac{\partial \mathbf{f}_m(\mathbf{u})}{\partial x_m} = 0, \quad (1)$$

where  $\mathbf{u}(\mathbf{x}, t) \in \mathbb{R}^n$  and  $\mathbf{f}_m : \mathbb{R}^n \rightarrow \mathbb{R}^n$  are the flux functions. We assume that (1) admits one or more entropy inequalities of the form

$$\frac{\partial S(\mathbf{u})}{\partial t} + \sum_{m=1}^d \frac{\partial F_m(\mathbf{u})}{\partial x_m} \leq 0, \quad (2)$$

where  $S(\mathbf{u})$  is a scalar convex entropy and  $F_m(\mathbf{u})$  are the associated entropy fluxes. The entropy variables are defined by

$$\mathbf{v}(\mathbf{u}) = \frac{\partial S}{\partial \mathbf{u}},$$

and for sufficiently regular solutions, one can derive the equality version of (2) by multiplying (1) by the entropy variables  $\mathbf{v}$ , using the chain rule and the following compatibility condition for the entropy and entropy fluxes

$$\mathbf{v}^T \frac{\partial \mathbf{f}_m}{\partial \mathbf{u}} = \frac{\partial F_m}{\partial \mathbf{u}}, \quad m = 1, \dots, d. \quad (3)$$

Furthermore, the entropy fluxes can be written as

$$F_m(\mathbf{u}) = \mathbf{v}(\mathbf{u})^T \mathbf{f}_m(\mathbf{u}) - \psi_m(\mathbf{u}), \quad (4)$$

where  $\psi_m(\mathbf{u})$  are the entropy potentials. Differentiating (4) and applying (3) yields

$$\frac{\partial \psi_m}{\partial \mathbf{u}}(\mathbf{u}) = \frac{\partial \mathbf{v}}{\partial \mathbf{u}}(\mathbf{u})^T \mathbf{f}_m(\mathbf{u}). \quad (5)$$

The decomposition of the entropy flux into entropy variables and a potential term is standard in the design of entropy-conservative and entropy-stable numerical schemes [67]. Finally, the convexity of  $S(\mathbf{u})$  guarantees that the mapping between conservative variables  $\mathbf{u}$  and entropy variables  $\mathbf{v}$  is invertible, and that the system is symmetrizable [27, 31].

A vanishing viscosity argument yields the inequality version of (2) for more general classes of solutions [19, 27, 37]. In this work, we utilize an integrated cell version of (2) [43]. Consider a closed domain  $D \subset \mathbb{R}^d$  with boundary  $\partial D$ . Integrating (2) over  $D$  and applying the divergence theorem yields

$$\int_D \frac{\partial S(\mathbf{u})}{\partial t} + \int_{\partial D} \sum_{m=1}^d (\mathbf{v}^T \mathbf{f}_m(\mathbf{u}) - \psi_m(\mathbf{u})) n_m \leq 0. \quad (6)$$

We will enforce this cell entropy inequality (6) by enforcing an intermediate identity. To derive this intermediate inequality, first multiply (1) by the entropy variables and integrate over some domain  $D$ . Integrating the spatial derivative term by parts yields

$$\int_D \frac{\partial S(\mathbf{u})}{\partial t} + \sum_{m=1}^d \left[ \int_D -\frac{\partial \mathbf{v}(\mathbf{u})^T}{\partial x_m} \mathbf{f}_m(\mathbf{u}) + \int_{\partial D} \mathbf{v}(\mathbf{u})^T \mathbf{f}_m(\mathbf{u}) n_m \right] = 0. \quad (7)$$

Subtracting (6) from (7) then yields

$$\sum_{m=1}^d \left( \int_D -\frac{\partial \mathbf{v}(\mathbf{u})^T}{\partial x_m} \mathbf{f}_m(\mathbf{u}) + \int_{\partial D} \psi_m(\mathbf{u}) n_m \right) \geq 0. \quad (8)$$

We note that for differentiable  $\mathbf{u}$  and  $\mathbf{f}_m(\mathbf{u})$ , (8) should be an *equality* due to (5)

$$\sum_{m=1}^d \left( \int_D -\frac{\partial \mathbf{v}(\mathbf{u})^T}{\partial x_m} \mathbf{f}_m(\mathbf{u}) + \int_{\partial D} \psi_m(\mathbf{u}) n_m \right) = 0. \quad (9)$$

### 3. Local discontinuous Galerkin (LDG) discretization of artificial viscosity

#### 3.1. High order DG formulation

We assume that the domain  $\Omega \subset \mathbb{R}^d$  is triangulated by non-overlapping simplicial elements  $D^k$ , where each element  $D^k$  is the image of a reference simplex  $\widehat{D}$  under some affine mapping  $\phi^k : \widehat{D} \rightarrow D^k$ . Let  $\mathbf{n}$  denote the outward normal vector  $\mathbf{n} = [n_1, \dots, n_d]$  on each face of  $D^k$ . Finally, let  $(u, v)_{D^k}, \langle u, v \rangle_{\partial D^k}$  denote the  $L^2$  inner products on  $D^k$  and the surface  $\partial D^k$

$$(u, v)_{D^k} \approx \int_{D^k} u(\mathbf{x})v(\mathbf{x}) dx, \quad \langle u, v \rangle_{\partial D^k} \approx \int_{\partial D^k} u(\mathbf{x})v(\mathbf{x}) dx,$$

where the approximate equality is due to the assumption that both volume and surface integrals in inner products are approximated using quadrature.

We consider a standard DG formulation for an approximate solution  $\mathbf{u}_h$  on a single element  $D^k$  for (1) [40, 45]:

$$\left( \frac{\partial \mathbf{u}_h}{\partial t}, \mathbf{w} \right)_{D^k} + \sum_{m=1}^d \left( -\mathbf{f}_m(\mathbf{u}_h), \frac{\partial \mathbf{w}}{\partial x_m} \right)_{D^k} + \langle \mathbf{f}_n^*, \mathbf{w} \rangle_{\partial D^k} = \mathbf{0}, \quad \mathbf{w} \in [P^N(D^k)]^n, \quad (10)$$

where  $P^N(D^k)$  denotes the space of total degree  $N$  polynomials on  $D^k$ . This formulation is derived by multiplying (1) by a test function  $\mathbf{w} \in [P^N(D^k)]^n$ , integrating by parts, and introducing a numerical flux  $\mathbf{f}_n^*$  across each inter-element interface. All volume and surface integrals are approximated using some quadrature rule, which will be specified later.

#### 3.2. Semi-discrete entropy estimate

First, we observe that for systems of nonlinear conservation laws, the entropy variables  $\mathbf{v}(\mathbf{u}_h)$  can be non-polynomial and do not necessarily lie in the test space  $[P^N(D^k)]^n$ . Thus, to derive a semi-discrete entropy estimate for (10), we must instead test with the  $L^2$  projection of the entropy variables  $\Pi_N \mathbf{v}(\mathbf{u}_h)$  [13, 14]. Here,  $\Pi_N$  denotes the  $L^2$  projection operator onto  $P^N(D^k)$  such that for  $f \in L^2(D^k)$

$$(\Pi_N f, v)_{D^k} = (f, v)_{D^k}, \quad \forall v \in P^N(D^k).$$

We note that similar observations on the non-polynomial nature of the entropy variables have been made by a variety of different groups in the literature [4, 17, 26, 35, 71].

Since  $\frac{\partial \mathbf{u}_h}{\partial t} \in [P^N(D^k)]^n$  for method of lines discretizations, testing the time derivative term in (10) with the projected entropy variables yields

$$\left( \frac{\partial \mathbf{u}_h}{\partial t}, \Pi_N \mathbf{v}(\mathbf{u}_h) \right)_{D^k} = \left( \frac{\partial \mathbf{u}_h}{\partial t}, \mathbf{v}(\mathbf{u}_h) \right)_{D^k} = \left( \frac{\partial S(\mathbf{u}_h)}{\partial t}, 1 \right)_{D^k}, \quad (11)$$

where we have used the chain rule in time for the final step. Note that this equality still holds under inexact quadrature, so long as the  $L^2$  projection operator  $\Pi_N$  is defined using the same inexact quadrature rule.

Considering (10) tested with the projected entropy variables and using (11), we recover the semi-discrete local rate of change of entropy of  $D^k$

$$\left( \frac{\partial S(\mathbf{u}_h)}{\partial t}, 1 \right)_{D^k} + \sum_{m=1}^d \left( -\mathbf{f}_m(\mathbf{u}_h), \frac{\partial \Pi_N \mathbf{v}(\mathbf{u}_h)}{\partial x_m} \right)_{D^k} + \langle \mathbf{f}_n^*, \Pi_N \mathbf{v}(\mathbf{u}_h) \rangle_{\partial D^k} = 0. \quad (12)$$

Due to the presence of the projected entropy variables and the fact that the inner products are approximated using quadrature, integration by parts, the chain rule, cannot be used to reproduce the proof of the continuous entropy (in)equality at the semi-discrete level from the DG formulation (12). In [14], a Laplacian artificial viscosity term is added to the high order DG method and discretized using BR-1 to recover an entropy inequality. In this work we discretize the artificial viscosity term with local DG [23, 25] instead, which allows us to derive an upper bound on the artificial viscosity coefficient that is not achieved under a BR-1 viscous discretization.

### 3.3. An entropy dissipative viscous LDG formulation

We consider adding the following Laplacian artificial viscosity term to (1)

$$\frac{\partial \mathbf{u}}{\partial t} + \sum_{m=1}^d \frac{\partial \mathbf{f}_m(\mathbf{u})}{\partial x_m} = \sum_{i,j=1}^d \frac{\partial}{\partial x_i} \left( \epsilon_k(\mathbf{u}) \frac{\partial \mathbf{u}}{\partial x_j} \right), \quad (13)$$

where  $\epsilon_k(\mathbf{u}) \geq 0$ . Applying the chain rule, (13) can be written as:

$$\frac{\partial \mathbf{u}}{\partial t} + \sum_{m=1}^d \frac{\partial \mathbf{f}_m(\mathbf{u})}{\partial x_m} = \sum_{i=1}^d \frac{\partial}{\partial x_i} \left( \epsilon_k(\mathbf{u}) \frac{\partial \mathbf{u}}{\partial \mathbf{v}} \frac{\partial \mathbf{v}}{\partial x_i} \right). \quad (14)$$

By the convexity of  $S(\mathbf{u})$ , the Jacobian matrix  $\frac{\partial \mathbf{u}}{\partial \mathbf{v}}$  is symmetric and positive definite. We will analyze the slightly more general viscous regularization:

$$\frac{\partial \mathbf{u}}{\partial t} + \sum_{m=1}^d \frac{\partial \mathbf{f}_m(\mathbf{u})}{\partial x_m} = \sum_{i,j=1}^d \frac{\partial}{\partial x_i} \left( \epsilon_k(\mathbf{u}) \mathbf{K}_{ij} \frac{\partial \mathbf{v}}{\partial x_j} \right), \quad (15)$$

where  $\mathbf{K}_{ij}$  denotes blocks of a symmetric and positive semi-definite matrix  $\mathbf{K}$

$$\mathbf{K} = \begin{bmatrix} \mathbf{K}_{11} & \cdots & \mathbf{K}_{1d} \\ \vdots & \ddots & \vdots \\ \mathbf{K}_{d1} & \cdots & \mathbf{K}_{dd} \end{bmatrix} = \mathbf{K}^T, \quad \mathbf{K} \succeq 0.$$

For example, taking  $\mathbf{K}_{ij} = \delta_{ij} \frac{\partial \mathbf{u}}{\partial \mathbf{v}}$  recovers (14). We discretize (15) by adding  $\mathbf{g}_{\text{visc}}$  to the DG formulation

$$\left( \frac{\partial \mathbf{u}_h}{\partial t}, \mathbf{w} \right)_{D^k} + \sum_{m=1}^d \left( -\mathbf{f}_m(\mathbf{u}_h), \frac{\partial \mathbf{w}}{\partial x_m} \right)_{D^k} + \langle \mathbf{f}_n^*, \mathbf{w} \rangle_{\partial D^k} = (\mathbf{g}_{\text{visc}}, \mathbf{w})_{D^k}, \quad (16)$$

where the viscous terms  $\mathbf{g}_{\text{visc}}$  are discretizations of (15) using a local DG discretization. Denoting

$\mathbf{v}_h = \Pi_N \mathbf{v}(\mathbf{u}_h)$ , the viscous terms  $\mathbf{g}_{\text{visc}}$  are given for  $i = 1, \dots, d$  by

$$(\Theta_i, \mathbf{w}_{1,i})_{D^k} = \left( -\mathbf{v}_h, \frac{\partial \mathbf{w}_{1,i}}{\partial x_i} \right)_{D^k} + \left\langle \left( \{\!\{ \mathbf{v}_h \}\!\} - \frac{\beta}{2} \llbracket \mathbf{v}_h \rrbracket \right) n_i, \mathbf{w}_{1,i} \right\rangle_{\partial D^k}, \quad \forall \mathbf{w}_{1,i} \in [P^N(D^k)]^n \quad (17)$$

$$(\sigma_i, \mathbf{w}_{2,i})_{D^k} = \left( \sum_{j=1}^d \epsilon_k(\mathbf{u}_h) \mathbf{K}_{ij} \Theta_j, \mathbf{w}_{2,i} \right)_{D^k}, \quad \forall \mathbf{w}_{2,i} \in [P^N(D^k)]^n \quad (18)$$

$$(\mathbf{g}_{\text{visc}}, \mathbf{w}_3)_{D^k} = \sum_{i=1}^d \left[ \left( -\sigma_i, \frac{\partial \mathbf{w}_3}{\partial x_i} \right)_{D^k} + \left\langle \left( \{\!\{ \sigma_i \}\!\} + \frac{\beta}{2} \llbracket \sigma_i \rrbracket \right) n_i, \mathbf{w}_3 \right\rangle_{\partial D^k} \right], \quad \forall \mathbf{w}_3 \in [P^N(D^k)]^n. \quad (19)$$

Here,  $\llbracket \cdot \rrbracket$  and  $\{\!\{ \cdot \}\!\}$  denote the jump and average operations:

$$\llbracket u \rrbracket = u^+ - u^-, \quad \{\!\{ u \}\!\} = \frac{1}{2} (u^+ + u^-),$$

where  $u^-$  denotes the interior value of  $u$  on a face of  $D^k$ , and  $u^+$  denotes the exterior (neighboring) value of  $u$  across the same face. Here,  $\Theta_i$  are DG approximations of derivatives of the entropy variables  $\mathbf{v}(\mathbf{u}_h)$  with respect to the  $i$ th coordinate. In (18), we compute the viscous fluxes  $\sigma_i$  as the  $L^2$  projection of  $\sum_{j=1}^d \mathbf{K}_{ij} \Theta_j$  for  $i = 1, \dots, d$  onto the approximation space of each element. The viscous terms  $\mathbf{g}_{\text{visc}}$  are the result of computing the divergence of the viscous fluxes in (19).

Additionally, let  $\beta$  be LDG parameters which are constant over each face. In this work, we define  $\beta = \text{sign}(\mathbf{v}_0 \cdot \mathbf{n})$ , where  $\mathbf{v}_0 \in \mathbb{R}^d$  is some fixed vector [23]. Setting  $\beta = 0$  recovers the BR-1 formulation. We note that LDG can also be equivalently defined in terms of binary ‘‘switches’’ [54]; both definitions of  $\beta$  fall under the general formulation in [25] and yield the same energy estimates.

The following lemma characterizes the global entropy dissipation estimate satisfied by (16). The proof is similar to proofs given in [14, 16], and is included for completeness.

**Lemma 1.** *Let  $\mathbf{g}_{\text{visc}}$  be given by (17), (18), and (19). Then, for a periodic domain,*

$$\sum_k -(\mathbf{g}_{\text{visc}}, \Pi_N \mathbf{v}(\mathbf{u}_h))_{D^k} = \sum_k \sum_{i,j=1}^d (\epsilon_k(\mathbf{u}_h) \mathbf{K}_{ij} \Theta_j, \Theta_i)_{D^k} \geq 0.$$

where  $\Pi_N \mathbf{v}(\mathbf{u}_h)$  denotes the  $L^2$  projection of the entropy variables.

*Proof.* Let  $\mathbf{w}_{1,i} = \sigma_i$ , integrate the volume term in (17) by parts, let  $\mathbf{w}_{2,i} = \Theta_i$ ,  $\mathbf{w}_3 = \mathbf{v}_h$ , and sum (17) and (18) from 1 to  $d$  to get

$$\sum_{i=1}^d (\Theta_i, \sigma_i)_{D^k} = \sum_{i=1}^d \left( \frac{\partial \mathbf{v}_h}{\partial x_i}, \sigma_i \right)_{D^k} + \left\langle \frac{1}{2} (\llbracket \mathbf{v}_h \rrbracket (1 - \beta)) n_i, \sigma_i \right\rangle_{\partial D^k}, \quad (20)$$

$$\sum_{i=1}^d (\sigma_i, \Theta_i)_{D^k} = \left( \sum_{i,j=1}^d \epsilon_k(\mathbf{u}_h) \mathbf{K}_{ij} \Theta_j, \Theta_i \right)_{D^k}, \quad (21)$$

$$(\mathbf{g}_{\text{visc}}, \mathbf{v}_h)_{D^k} = \sum_{i=1}^d \left[ \left( -\sigma_i, \frac{\partial \mathbf{v}_h}{\partial x_i} \right)_{D^k} + \left\langle \left( \{\!\{ \sigma_i \}\!\} + \frac{\beta}{2} \llbracket \sigma_i \rrbracket \right) n_i, \mathbf{v}_h \right\rangle_{\partial D^k} \right]. \quad (22)$$

Substituting (20) into (22) and summing over  $D^k$  shows that  $\sum_k (\mathbf{g}_{\text{visc}}, \mathbf{v}_h)_{D^k}$  is equal to

$$\sum_k \sum_{i,j=1} (-\boldsymbol{\Theta}_i, \boldsymbol{\sigma}_i)_{D^k} + \left\langle \left( \frac{1}{2} \llbracket \mathbf{v}_h \rrbracket (1 - \beta) \right) n_i, \boldsymbol{\sigma}_i \right\rangle_{\partial D^k} + \left\langle \left( \{\{\boldsymbol{\sigma}_i\}\} + \frac{\beta}{2} \llbracket \boldsymbol{\sigma}_i \rrbracket \right) n_i, \mathbf{v}_h \right\rangle_{\partial D^k}$$

Summing (21) over the elements and substituting into the equation above we have

$$\begin{aligned} \sum_k (\mathbf{g}_{\text{visc}}, \mathbf{v}_h)_{D^k} &= \sum_k \sum_{i,j=1} -(\epsilon_k(\mathbf{u}_h) \mathbf{K}_{ij} \boldsymbol{\Theta}_j, \boldsymbol{\Theta}_i)_{D^k} \\ &+ \left\langle \left( \frac{1}{2} \llbracket \mathbf{v}_h \rrbracket (1 - \beta) \right) n_i, \boldsymbol{\sigma}_i \right\rangle_{\partial D^k} + \left\langle \left( \{\{\boldsymbol{\sigma}_i\}\} + \frac{\beta}{2} \llbracket \boldsymbol{\sigma}_i \rrbracket \right) n_i, \mathbf{v}_h \right\rangle_{\partial D^k} \end{aligned} \quad (23)$$

For periodic boundary conditions, all faces are ‘‘interior’’ faces share by two elements. We split the contributions from each surface term and swap them between  $D^k$  and the neighboring element  $D^{k,+}$ , and rearrange the boundary terms noting that  $n_i$ ,  $\llbracket \mathbf{v}_h \rrbracket$ , and  $\beta$  change sign between  $D^k$  and  $D^{k,+}$ . The first surface term from (23) is

$$\begin{aligned} &\frac{1}{2} \sum_k \langle (\llbracket \mathbf{v}_h \rrbracket (1 - \beta)) n_i, \boldsymbol{\sigma}_i \rangle_{\partial D^k} \\ &= \frac{1}{2} \sum_k \left( \frac{1}{2} \langle \llbracket \mathbf{v}_h \rrbracket (1 - \beta) n_i, \boldsymbol{\sigma}_i \rangle_{\partial D^k} + \left\langle \frac{1}{2} \llbracket \mathbf{v}_h \rrbracket (1 - \beta) n_i, \boldsymbol{\sigma}_i \right\rangle_{\partial D^{k,+}} \right) \\ &= \frac{1}{2} \sum_k \left\langle \left( \{\{\boldsymbol{\sigma}_i\}\} + \frac{\beta}{2} \llbracket \boldsymbol{\sigma}_i \rrbracket \right) n_i, \llbracket \mathbf{v}_h \rrbracket \right\rangle \end{aligned}$$

The second surface term from (23) is

$$\begin{aligned} &\sum_k \left\langle \left( \{\{\boldsymbol{\sigma}_i\}\} + \frac{\beta}{2} \llbracket \boldsymbol{\sigma}_i \rrbracket \right) n_i, \mathbf{v}_h \right\rangle_{\partial D^k} \\ &= \frac{1}{2} \sum_k \left( \left\langle \left( \{\{\boldsymbol{\sigma}_i\}\} + \frac{\beta}{2} \llbracket \boldsymbol{\sigma}_i \rrbracket \right) n_i, \mathbf{v}_h \right\rangle_{\partial D^k} + \left\langle \left( \{\{\boldsymbol{\sigma}_i\}\} + \frac{\beta}{2} \llbracket \boldsymbol{\sigma}_i \rrbracket \right) n_i, \mathbf{v}_h \right\rangle_{\partial D^{k,+}} \right) \\ &= -\frac{1}{2} \sum_k \left\langle \left( \{\{\boldsymbol{\sigma}_i\}\} + \frac{\beta}{2} \llbracket \boldsymbol{\sigma}_i \rrbracket \right) n_i, \frac{1}{2} \llbracket \mathbf{v}_h \rrbracket \right\rangle_{\partial D^k}. \end{aligned}$$

Thus, the two surface terms cancel and by the positive semi-definiteness of  $\mathbf{K}_{ij}$ , we have

$$-\sum_k (\mathbf{g}_{\text{visc}}, \mathbf{v}_h)_{D^k} = \sum_k \sum_{i,j=1} (\epsilon_k(\mathbf{u}_h) \mathbf{K}_{ij} \boldsymbol{\Theta}_j, \boldsymbol{\Theta}_i)_{D^k} \leq 0. \quad (24)$$

□

Note that the LDG dissipation estimate in Lemma 1 is exactly the same as the dissipation estimate for BR-1. Thus, Lemma 2 in [14] holds for both BR-1 and LDG, which we restate without proof below:

**Lemma 2** (Lemma 2 in [14]). Let  $\epsilon_k(\mathbf{u}_h)$  on  $D^k$  satisfy

$$\sum_{i,j=1}^d (\epsilon_k(\mathbf{u}_h) \mathbf{K}_{ij} \boldsymbol{\Theta}_j, \boldsymbol{\Theta}_i)_{D^k} \geq -\min(0, \delta_k(\mathbf{u}_h)), \quad (25)$$

where the volume entropy residual  $\delta_k(\mathbf{u}_h)$  is

$$\delta_k(\mathbf{u}_h) = \sum_{m=1}^d \left[ \left( -\mathbf{f}_m(\mathbf{u}_h), \frac{\partial \Pi_N \mathbf{v}_h}{\partial x_m} \right)_{D^k} + \langle \psi_m(\tilde{\mathbf{u}}) n_m, 1 \rangle_{\partial D^k} \right]. \quad (26)$$

Let  $\tilde{\mathbf{u}}$  denotes the entropy projection  $\tilde{\mathbf{u}} = \mathbf{u}(\Pi_N \mathbf{v}(\mathbf{u}_h))$ , and assume the numerical flux  $\mathbf{f}_n^*$  is evaluated in terms of the entropy projection. Then, (16) satisfies the following global entropy inequality:

$$\sum_k \left[ \left( \frac{\partial S(\mathbf{u}_h)}{\partial t}, 1 \right)_{D^k} + \left\langle (\Pi_N \mathbf{v}(\mathbf{u}_h))^T \mathbf{f}_n^* - \sum_{m=1}^d \psi_m(\tilde{\mathbf{u}}) n_m, 1 \right\rangle_{\partial D^k} \right] \leq 0. \quad (27)$$

We note that under nodal collocation of both volume and surface quadratures, the evaluation of the entropy projection  $\tilde{\mathbf{u}}$  reduces to the evaluation of the polynomial DG solution  $\mathbf{u}_h$  at interfaces.

Finally, a simple expression for the ECAV coefficient can be given by assuming that  $\epsilon_k(\mathbf{u}_h)$  is constant over each element:

$$\epsilon_k(\mathbf{u}_h) = \frac{-\min(0, \delta_k(\mathbf{u}_h))}{\sum_{i,j=1}^d (\mathbf{K}_{ij} \boldsymbol{\Theta}_j, \boldsymbol{\Theta}_i)_{D^k}}, \quad (28)$$

where we approximate the ratio above via

$$\frac{a}{b} \approx \frac{ab}{b^2 + \delta}. \quad (29)$$

Unless otherwise specified, we arbitrarily take  $\delta = 10^{-14}$  for the experiments in this work.

#### 4. Properties of ECAV under LDG

The main contributions of this paper are to provide an upper bound based on (28) and properties of the LDG discretization. The motivation for the use of the LDG discretization in (20) is the availability of estimates for the gradient which do not hold for BR-1. These estimates enable an upper bound on the ECAV coefficient.

##### 4.1. Estimates for the LDG gradient

Let  $V^N(D^k)$  denote the local approximation space on the element  $D^k$ . On simplices,  $V^N(D^k) = P^N(D^k)$ , while on quadrilateral or hexahedral elements,  $V^N(D^k) = Q^N(D^k)$ . The LDG gradient of a scalar quantity  $u$  can be defined locally (integrating (17) by parts) as

$$(\boldsymbol{\theta}, \mathbf{w})_{D^k} = (\nabla u, \mathbf{w})_{D^k} + \left\langle \frac{1}{2} \llbracket u \rrbracket (1 - \beta), \mathbf{w} \cdot \mathbf{n} \right\rangle_{\partial D^k} \quad \forall \mathbf{w} \in [V^N(D^k)]^d, \quad (30)$$

where  $\beta = \text{sign}(\mathbf{v}_0 \cdot \mathbf{n})$  for some divergence-free  $\mathbf{v}_0 \in \mathbb{R}^d$ .

Let  $a \lesssim b$  denote  $a \leq Cb$  where  $C$  is independent of the mesh size (though it may depend on shape regularity and polynomial degree). Restricting for the moment to the case when  $D^k$  is an affine simplex, we have the following lemma:

**Lemma 3.** *Let  $D^k$  be a  $d$ -dimensional affine simplex and  $\beta = 1$  on at least one face. Then,*

$$\|\boldsymbol{\theta}\|_{L^2(D^k)} \gtrsim \|\nabla u\|_{L^2(D^k)}.$$

*Proof.* To show this bound, we choose  $\mathbf{w}$  in (30) to be some projection  $\boldsymbol{\tau}^* \in P^N(D^k)$ . We use the projection from Section 3.1 of [23]

$$\begin{aligned} (\boldsymbol{\tau}^*, \mathbf{w})_{D^k} &= (\nabla u, \mathbf{w}), & \forall \mathbf{w} \in [P^{N-1}(D^k)]^d, \\ \langle \boldsymbol{\tau}^* \cdot \mathbf{n}, w \rangle_f &= \langle 0, w \rangle_f, & \forall w \in P^N(\partial D^k \setminus f^*) \quad i = 1, \dots, d-1 \end{aligned} \quad (31)$$

where  $f^*$  denotes a single face for which  $\beta = 1$ . Note that, if  $\beta = \text{sign}(\mathbf{v}_0 \cdot \mathbf{n})$  for a locally constant (or more generally, a divergence-free  $\mathbf{v}_0$ ), then for affine simplices, at least one such face where  $\beta = 1$  must exist [23]. Next, we note that  $\|\boldsymbol{\theta}\|_{L^2(D^k)}$  can be expressed as a supremum [44]

$$\|\boldsymbol{\theta}\|_{L^2(D^k)} = \sup_{\mathbf{w} \in [P^N D^k / \{0\}]^d} \frac{(\boldsymbol{\theta}, \mathbf{w})_{D^k}}{\|\mathbf{w}\|_{L^2(D^k)}}.$$

Then, testing with  $\boldsymbol{\tau}^*$  given by (31), it follows that

$$\|\boldsymbol{\theta}\|_{L^2(D^k)} = \sup_{\mathbf{w} \in [P^N D^k / \{0\}]^d} \frac{(\boldsymbol{\theta}, \mathbf{w})_{D^k}}{\|\mathbf{w}\|_{L^2(D^k)}} \gtrsim \frac{(\boldsymbol{\theta}, \boldsymbol{\tau}^*)}{\|\boldsymbol{\tau}^*\|_{L^2(D^k)}} \gtrsim \|\nabla u\|_{L^2(D^k)},$$

where we have used in the final step that  $(\boldsymbol{\theta}, \boldsymbol{\tau}^*)_{D^k} = \|\nabla u\|_{L^2(D^k)}^2$  from (31) and that  $\|\boldsymbol{\tau}^*\|_{L^2(D^k)} \lesssim \|\nabla u\|_{L^2(D^k)}$  by Lemma 3.2 in [23].  $\square$

**Remark 1.** *While Lemma 3 only holds for simplices, the generalization to Cartesian quadrilateral or hexahedral elements can be performed using a tensor product version of this projection with similar properties; see (3.4-3.5) of [24]. Additionally, the proof is straightforward to extend to curved elements if  $\beta = 1$  on at least one face.*

We note that Lemma 3 implies that the LDG gradient is locally null-space consistent, in that the nullspace of the LDG gradient operator is spanned only by the constant. This distinguishes LDG from other stabilized discretizations [5], which focus on null-space consistency of the discretized Laplacian as opposed to the gradient. We also note that, while Cockburn and Dong showed that the more general LDG fluxes where  $\text{sign}(\beta) = \text{sign}(\mathbf{v}_0 \cdot \mathbf{n})$  also result in a well-posed discretization of the Laplacian [23], they do not imply local null-space consistency of the gradient in general.

#### 4.2. Upper bounds on the ECAV artificial viscosity coefficient

Recall that the ECAV artificial viscosity coefficient is defined as

$$\epsilon_k(\mathbf{u}_h) = \frac{-\min(0, \delta_k(\mathbf{u}_h))}{\int_{D^k} \boldsymbol{\theta}^T \mathbf{K} \boldsymbol{\theta}}$$

where the volume entropy residual  $\delta_k(\mathbf{u}_h)$  is

$$\delta_k(\mathbf{u}_h) = \sum_{i=1}^d \int_{D^k} -\mathbf{f}_i(\mathbf{u}_h) \frac{\partial \Pi_N \mathbf{v}(\mathbf{u}_h)}{\partial x_i} + \int_{\partial D^k} \psi_i(\tilde{\mathbf{u}}) n_i.$$

Here,  $\psi_i(\mathbf{u})$  is the entropy potential and  $\tilde{\mathbf{u}} = \mathbf{u}(\Pi_N \mathbf{v}(\mathbf{u}_h))$  is the entropy projection (e.g., the evaluation of the conservative variables using the  $L^2$  projection of the entropy variables).

Using properties of the LDG gradient, we can bound the artificial viscosity from above. We first make the following assumption:

**Assumption 1.** *The solution  $\mathbf{u}_h$  is defined such that the dissipation matrices  $\mathbf{K}_{ij}$  are pointwise positive-definite*

$$\sum_{i,j=1}^d \boldsymbol{\Theta}_i^T \mathbf{K}_{ij} \boldsymbol{\Theta}_j \geq \lambda_{\min} \sum_{i=1}^d \boldsymbol{\Theta}_i^T \boldsymbol{\Theta}_i.$$

For the Laplacian artificial viscosity in this work, this corresponds to the condition that  $\frac{\partial \mathbf{u}}{\partial \mathbf{v}}$  is positive-definite. This holds if the entropy  $S(\mathbf{u})$  is strongly convex, and is equivalent to the density and internal energy being bounded from below by some positive value.

**Lemma 4.** *Let Assumption 1 hold, and assume exact integration of all integrals in the DG formulation (16) and that  $\tilde{\mathbf{u}}, \mathbf{f}_m(\tilde{\mathbf{u}})$  are differentiable. Then, we have the following bound:*

$$\epsilon_k(\mathbf{u}_h) \lesssim C(\mathbf{u}_h)h$$

where  $C(\mathbf{u}_h)$  is given by

$$C(\mathbf{u}_h) = \|\lambda_{\min}^{-1}\|_{L^\infty} \sqrt{\sum_{i=1}^d \left\| \frac{\partial \mathbf{f}_i}{\partial \mathbf{v}} \right\|^2} \sqrt{\frac{\|\boldsymbol{\delta \mathbf{v}}\|_{L^2(D^k)}^2}{\|\Pi_N \boldsymbol{\delta \mathbf{v}}\|_{L^2(D^k)}^2} - 1}.$$

Here,  $\bar{\mathbf{v}}$  is the integral mean of  $\mathbf{v}(\mathbf{u}_h)$  over  $D^k$  and  $\boldsymbol{\delta \mathbf{v}} = \mathbf{v}(\mathbf{u}_h) - \bar{\mathbf{v}}$ .

*Proof.* By Assumption 1, we have that

$$\epsilon_k(\mathbf{u}_h) = \frac{-\min(0, \delta_k(\mathbf{u}_h))}{\int_{D^k} \boldsymbol{\theta}^T \mathbf{K} \boldsymbol{\theta}} \leq \|\lambda_{\min}^{-1}\|_{L^\infty} \frac{|\delta_k(\mathbf{u}_h)|}{\|\boldsymbol{\theta}\|_{L^2(D^k)}^2}.$$

Lemma 3 then yields

$$\frac{|\delta_k(\mathbf{u}_h)|}{\|\boldsymbol{\theta}\|_{L^2(D^k)}^2} \leq \frac{|\delta_k(\mathbf{u}_h)|}{\|\nabla \Pi_N \mathbf{v}(\mathbf{u}_h)\|_{L^2(D^k)}^2}. \quad (32)$$

We can bound the numerator  $\delta_k(\mathbf{u}_h)$  by noting that, since  $\tilde{\mathbf{u}}$  is defined in terms of the  $L^2$  projection of the entropy variables [14, 26], the solution is differentiable and from (9) the boundary integral of the entropy variables is equivalent to the following volume integral

$$\int_{\partial D^k} \psi_i(\tilde{\mathbf{u}}) n_i = \int_{D^k} -\mathbf{f}_i(\tilde{\mathbf{u}})^T \frac{\partial \Pi_N \mathbf{v}(\mathbf{u}_h)}{\partial x_i}.$$

Thus, factoring out derivatives of the projected entropy variables and using Cauchy-Schwarz yields

$$|\delta_k(\mathbf{u}_h)| \leq \sqrt{\sum_{i=1}^d \|\mathbf{f}_i(\mathbf{u}_h) - \mathbf{f}_i(\tilde{\mathbf{u}})\|_{L^2(D^k)}^2} \|\nabla \Pi_N \mathbf{v}(\mathbf{u}_h)\|_{L^2(D^k)}$$

Substituting this into (32), applying the mean value theorem, and factoring out the Jacobians  $\frac{\partial \mathbf{f}_i}{\partial \mathbf{v}}$  then yields

$$\epsilon_k(\mathbf{u}_h) \leq \sqrt{\sum_{i=1}^d \left\| \frac{\partial \mathbf{f}_i}{\partial \mathbf{v}} \right\|^2} \frac{\|\mathbf{v}(\mathbf{u}_h) - \Pi_N \mathbf{v}(\mathbf{u}_h)\|_{L^2(D^k)}}{\|\nabla \Pi_N \mathbf{v}(\mathbf{u}_h)\|_{L^2(D^k)}}$$

We bound the denominator from below using a discrete Poincare-Friedrichs inequality [10, 12]

$$h \|\nabla \Pi_N \mathbf{v}(\mathbf{u}_h)\|_{L^2(D^k)} \gtrsim \|\Pi_N \mathbf{v}(\mathbf{u}_h) - \bar{\mathbf{v}}\|_{L^2(D^k)}.$$

Next, we note that the  $L^2$  projection preserves constant moments, such that

$$\|\mathbf{v}(\mathbf{u}_h) - \Pi_N \mathbf{v}(\mathbf{u}_h)\|_{L^2(D^k)} = \|(\mathbf{v}(\mathbf{u}_h) - \bar{\mathbf{v}}) - \Pi_N (\mathbf{v}(\mathbf{u}_h) - \bar{\mathbf{v}})\|_{L^2(D^k)} = \|(\boldsymbol{\delta} \mathbf{v} - \Pi_N \boldsymbol{\delta} \mathbf{v})\|_{L^2(D^k)}.$$

The proof is completed by noting that, by  $L^2$  orthogonality of the projection error,  $\|u\|_{L^2}^2 = \|u - \Pi_N u\|_{L^2}^2 + \|\Pi_N u\|_{L^2}^2$  for any  $u \in L^2$ , and that

$$\frac{\|u - \Pi_N u\|_{L^2}^2}{\|\Pi_N u\|_{L^2}^2} = \frac{\|u\|_{L^2}^2 - \|\Pi_N u\|_{L^2}^2}{\|\Pi_N u\|_{L^2}^2} = \frac{\|u\|_{L^2}^2}{\|\Pi_N u\|_{L^2}^2} - 1.$$

□

We note that, since the  $L^2$  projection is contractive in the  $L^2$  norm, the ratio of norms  $\frac{\|\boldsymbol{\delta} \mathbf{v}\|_{L^2(D^k)}^2}{\|\Pi_N \boldsymbol{\delta} \mathbf{v}\|_{L^2(D^k)}^2} \geq 1$ . However, numerical experiments suggest that this quantity is typically very close to 1, even in the presence of shocks or near-zero density or pressure (which result in the entropy variable mapping being nearly singular and ill-conditioned).

**Remark 2** (On quadrature accuracy). *We also note that, while Lemma 4 assumes exact integration, for sufficiently accurate quadrature<sup>1</sup>, the quadrature error is of the same order of magnitude as the volume entropy residual  $\delta_k(\mathbf{u}_h)$ . Moreover, we emphasize that the ECAV coefficient (28) is designed so that the formulation (16) is guaranteed to satisfy an entropy inequality independent of the choice of quadrature, and that quadrature accuracy affects only the magnitude of  $\epsilon_k(\mathbf{u}_h)$ .*

*Accounting for quadrature accuracy is also necessary when analyzing systems of conservation laws under the square entropy  $S(\mathbf{u}) = \frac{1}{2} \mathbf{u}^T \mathbf{u}$ , as  $\mathbf{v}(\mathbf{u}) = \mathbf{u}$ , as the entropy variables are identical to the conservative variables and the factor  $\|\mathbf{v}(\mathbf{u}_h) - \Pi_N \mathbf{v}(\mathbf{u}_h)\|_{D^k}$  in Lemma 4 would vanish. This reflects the fact that DG discretizations of systems which are symmetrizable by a square entropy are automatically entropy stable under exact integration. Thus, while the bound in Lemma 4 still holds, it is not practically useful for such settings.*

Finally, we note that Lemma 4 provides a pessimistic upper bound on the magnitude of  $\epsilon_k(\mathbf{u}_h)$ . However, for sufficiently regular solutions, we expect  $\epsilon_k(\mathbf{u}_h)$  to be much smaller in magnitude. The beginning of the proof of Lemma 4 implies that

$$\epsilon_k(\mathbf{u}_h) = \frac{-\min(0, \delta_k(\mathbf{u}_h))}{\int_{D^k} \boldsymbol{\theta}^T \mathbf{K} \boldsymbol{\theta}} \lesssim \frac{|\delta_k(\mathbf{u}_h)|}{\|\nabla \Pi_N \mathbf{v}(\mathbf{u}_h)\|_{D^k}^2}.$$

<sup>1</sup>For example, if the volume quadrature is exact for degree  $2N + 1$  polynomials and the surface quadrature exact for degree  $2N + 2$  polynomials [14].

We now consider the behavior of  $\epsilon_k(\mathbf{u}_h)$  as  $\mathbf{u}_h \rightarrow \mathbf{u}$  under mesh refinement for some fixed sufficiently regular function  $\mathbf{u}$ . For regions where  $\mathbf{u}$  is not constant, the denominator will converge to a positive value under mesh refinement. When  $\mathbf{u}_h$  is exactly constant over  $D^k$ ,  $\epsilon_k(\mathbf{u}_h) = 0$  when calculated using the regularized ratio (29) since both the denominator and numerator vanish. Thus, what remains is to consider the case when  $\nabla \mathbf{u}$  vanishes only at specific points (or over a surface) within an element. For such cases, applying a discrete Poincare-Friedrichs inequality [10, 12] yields

$$\epsilon_k(\mathbf{u}_h) \lesssim \frac{|\delta_k(\mathbf{u}_h)|}{\|\nabla \Pi_N \mathbf{v}(\mathbf{u}_h)\|_{D^k}^2} \lesssim h^2 \frac{|\delta_k(\mathbf{u}_h)|}{\|\Pi_N(\mathbf{v}(\mathbf{u}_h) - \bar{\mathbf{v}})\|_{D^k}^2}.$$

It was shown in [14] that the numerator is  $O(h^{2N+2+d})$  under exact integration. Assuming that  $\nabla \mathbf{u}$  vanishes inside  $D^k$  (but is not identically zero),  $\mathbf{v}(\mathbf{u}_h) - \bar{\mathbf{v}} = O(h)$  and the denominator is  $O(h^{2+d})$ . Together, this suggests that  $\max_k \epsilon_k(\mathbf{u}_h) \lesssim O(h^{2N+2})$  for sufficiently regular solutions, which is consistent with numerical results presented in [14] for sufficiently accurate quadrature.

## 5. Numerical experiments

In this section, we present numerical experiments which confirm theoretical properties of ECAV under an LDG discretization of (13), compared to a BR-1 type regularization used in [14]. All experiments are implemented in Julia using the `StartUpDG.jl` and `Trixi.jl` [60] libraries. For the following 1D experiments, nodal collocation formulations use a  $(N + 1)$ -point Gauss-Lobatto quadrature rule, while modal formulations use a  $(N + 2)$ -point Gauss-Legendre quadrature rule. Unless otherwise stated, we use the HLLC interface flux [7]. Finally, the parameter  $\beta$  for the LDG discretization in Equation (17) and Equation (19) is chosen as  $\beta = \text{sgn}(n_x)$  and  $\beta = \text{sgn}(2n_x + n_y)$  for 1D and 2D experiments, respectively.

For time integration, we use the `OrdinaryDiffEq.jl` library [57]. Unless stated otherwise, we use the adaptive 4-stage 3rd order strong stability preserving Runge-Kutta method (SSPRK43) [29, 48, 59] with absolute and relative tolerances set to  $10^{-6}$  and  $10^{-4}$ , respectively.

Finally, we will consider two different formulations which result from different choices of quadrature. Unless otherwise specified, we use a ‘‘modal’’ formulation with a  $(N + 2)$ -point Gauss-Legendre quadrature in 1D, and quadrature rules which are exact for degree  $2N$  polynomials on triangular elements.

### 5.1. 2D Inviscid Burgers Equation

We begin by comparing the magnitude of the entropy correction artificial viscosity coefficient using the BR-1 and LDG discretizations. Consider the 2D inviscid Burgers Equation

$$\frac{\partial u}{\partial t} + \frac{\partial}{\partial x} \left( \frac{1}{2} u^2 \right) + \frac{\partial}{\partial y} \left( \frac{1}{2} u^2 \right) = 0. \quad (33)$$

An initial boundary value problem is formulated on a domain of  $(x, y) \in [-1, 1]^2$ , with periodic boundary conditions, a Gaussian initial condition

$$u_0(x, y) = \exp(-25(x^2 + y^2)),$$

and a final time of  $t = 0.77$ . Equation (33) admits the following entropy functional with the associated entropy potentials

$$S(u) = \frac{u^2}{2}, \quad \psi_1(u) = \psi_2(u) = \frac{u^3}{6}.$$

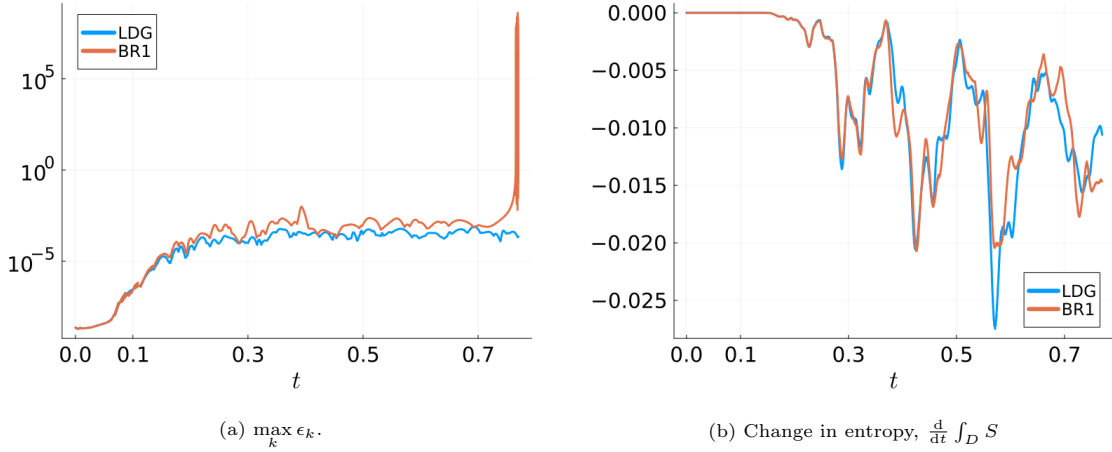


Figure 1: Example 5.1, time evolution of the  $\max_k \epsilon_k$  (semi-log plot) and change in entropy over time for BR-1 and LDG discretizations of the entropy correction artificial viscosity with  $N = 2$  and  $K = 2 \times 40^2$  elements.

We use polynomial order  $N = 3$ ,  $K = 2 \times 30^2$  triangular elements, and the entropy-conserving interface flux [33]

$$f_{\mathbf{n}}^*(u, u^+) = \frac{1}{6} \left( (u^+)^2 + u^- u^+ + (u^-)^2 \right) (n_1 + n_2).$$

In Figure 1 we observe that the rate of change of entropy is non-positive, implying that both entropy correction methods satisfy the entropy inequality. However the maximum artificial viscosity discretized with BR-1 is several orders of magnitude larger than the maximum artificial viscosity discretized with LDG. As a result, an adaptive SSPRK43 time integrator results in 474 adaptive time steps for LDG, compared to 20932 adaptive time steps for BR-1. We also analyzed the behavior of BR-1 and LDG under a nodal DG-like formulation constructed using multi-dimensional summation by parts (SBP) operators [41]. Under this nodal SBP formulation, LDG completes the simulation in 640 adaptive time steps, while the BR-1 discretization does not converge even after 100,000 time steps. We note that, due to  $\epsilon_k(\mathbf{u}_h)$  being large, BR-1 induces extremely small time steps on the order of  $10^{-10}$  starting at roughly  $t = 0.39897$ .

**Remark 3.** Under the BR-1 viscous discretization and a nodal DG formulation, computing the regularized ratio (29) with  $\delta = 10^{-14}$  resulted in violations of the semi-discrete entropy inequality due to finite precision effects. To address this issue, for both the nodal and modal DG formulations in this section, we use `eps(b)` for  $\delta$ , which returns the distance between  $\mathbf{b}$  and the next representable floating-point value larger than  $\mathbf{b}$ .

We do not observe a significant difference between BR-1 and LDG for this problem when using an entropy stable interface flux. However, while the use of an entropy conservative interface flux in these experiments is mainly intended to confirm our theoretical results, the use of non-dissipative interface fluxes in realistic simulations has been explored for applications in turbulence modeling [30].

## 5.2. Compressible Euler Equations

The remaining examples solve the 1D or 2D compressible Euler equations which are described below. Let  $\mathbf{u}$  denote the vector of conserved variables, which in 2D are

$$\mathbf{u} = \{\rho, \rho u_1, \rho u_2, E\} \in \mathbb{R}^4.$$

Here,  $\rho$  is the density,  $u_1$  and  $u_2$  are the velocity in the  $x$  and  $y$  direction, and  $E$  is the specific total energy. The pressure  $p$  is related to the conservative variables through the ideal gas constitutive relations

$$p = (\gamma - 1)\rho e, \quad E = e + \frac{1}{2}(u_1^2 + u_2^2),$$

where  $\gamma$  is the ratio of specific heats and  $e$  is the internal energy density. All problems in this work utilize  $\gamma = 1.4$  for calorically perfect air. In 2D the compressible Euler equations are

$$\frac{\partial \mathbf{u}}{\partial t} + \frac{\partial \mathbf{f}_1}{\partial x} + \frac{\partial \mathbf{f}_2}{\partial y} = \mathbf{0},$$

where  $\mathbf{f}_1$  and  $\mathbf{f}_2$  denote the convective fluxes in the  $x$  and  $y$  direction,

$$\mathbf{f}_1 = \begin{bmatrix} \rho u_1 \\ \rho u_1^2 + p \\ \rho u_1 u_2 \\ u_1(E + p) \end{bmatrix}, \quad \mathbf{f}_2 = \begin{bmatrix} \rho u_2 \\ \rho u_1 u_2 \\ \rho u_2^2 + p \\ u_2(E + p) \end{bmatrix}.$$

If the velocity is set to zero in the  $y$ -direction, the 1D compressible Euler equations are recovered by disregarding the  $y$ -momentum equation.

The convex entropy function  $\mathbf{v}(\mathbf{u}) = \frac{\partial S}{\partial \mathbf{u}}$  and corresponding entropy potentials  $\psi_1(\mathbf{u})$  and  $\psi_2(\mathbf{u})$

$$S(\mathbf{u}) = -\rho s, \quad \psi_1(\mathbf{u}) = \rho u_1, \quad \psi_2(\mathbf{u}) = \rho u_2,$$

where  $s = \log\left(\frac{p}{\rho^\gamma}\right)$  denotes the physical entropy. The derivative of the entropy with respect to the conservative variables yield the entropy variables  $\mathbf{v}(\mathbf{u}) = \frac{\partial S}{\partial \mathbf{u}} = \{v_1, v_2, v_3, v_4\}$ , where

$$v_1 = \frac{\rho e (\gamma + 1 - s)}{\rho e}, \quad v_2 = \frac{\rho u_1}{\rho e}, \quad v_3 = \frac{\rho u_2}{\rho e}, \quad v_4 = -\frac{\rho}{\rho e}.$$

The inverse mapping is given by

$$\rho = -(\rho e)v_4, \quad \rho u_1 = (\rho e)v_2, \quad \rho u_2 = (\rho e)v_3, \quad E = (\rho e) \left(1 - \frac{v_2^2 + v_3^4}{2v_4}\right),$$

and  $\rho e$  and  $s$  in terms of the entropy variables are

$$\rho e = \left(\frac{(\gamma - 1)}{(-v_4)}\right)^{1/(\gamma-1)} e^{\frac{-s}{\gamma-1}}, \quad s = \gamma - v_1 + \frac{v_2^2 + v_3^4}{2v_4}.$$

Finally, explicit expressions for the Jacobian matrix  $\frac{\partial \mathbf{u}}{\partial \mathbf{v}}$  are given in terms of the sound speed  $a$  and specific total enthalpy  $H$  [6].

$$\frac{\partial \mathbf{u}}{\partial \mathbf{v}} = \begin{bmatrix} \rho & \rho u_1 & \rho u_2 & E \\ \rho u_1^2 + p & \rho u_1 u_2 & u_1(E + p) & \\ & \rho u_2^2 + p & u_2(E + p) & \\ & & \rho H^2 - a^2 \frac{p}{\gamma - 1} & \end{bmatrix},$$

$$a = \sqrt{\gamma \frac{p}{\rho}}, \quad H = \frac{a^2}{\gamma - 1} + \frac{1}{2}(u_1^2 + u_2^2),$$

where the lower triangular entries of  $\frac{\partial \mathbf{u}}{\partial \mathbf{v}}$  are determined by symmetry.

### 5.3. Shu Isentropic Euler Vortex Problem

This problem appeared in [63] to compare high-order weighted essentially non-oscillatory (WENO) finite-volume (FV) methods with a traditional second-order FV method. Since then, many variations of the problem have been considered in the literature; see [65] and the references therein. This problem has an exact solution and we will use it to examine the accuracy of the proposed method. To reduce the effect of temporal discretization errors in our convergence results, we use the 5th-order accurate Runge-Kutta method of [68] (`Tsit5` in `OrdinaryDiffEq.jl`) instead of `SSPRK43`. The absolute tolerance is set to  $10^{-10}$  and the relative tolerance is set to  $10^{-8}$ .

The initial conditions for this problem are an isentropic vortex added to mean flow quantities. The mean flow quantities are  $\rho = p = 1$  and  $u_1 = u_2 = 1/\gamma$  and the isentropic vortex is added by perturbing  $u_1$ ,  $u_2$  and the temperature  $T = p/\rho$ , but not perturbing the entropy  $S = p/\rho^\gamma$ . These perturbations are

$$\begin{aligned} \delta u_1(x, y) &= -y\Omega(x, y), & \delta u_2(x, y) &= x\Omega(x, y), \\ \delta T(x, y) &= -\frac{(\gamma - 1)}{2}\Omega(x, y), & \Omega(x, y) &= \alpha \exp -\frac{1}{2}(x^2 + y^2), \end{aligned}$$

where  $\alpha = 5 \exp(1/2)/(2\pi\sqrt{\gamma})$  is the maximum strength of the perturbation. The analytical solution is a translation of the initial condition given by

$$\begin{aligned} \rho(x, y, t) &= \tilde{\rho}\left(x - \frac{1}{\gamma}t, y - \frac{1}{\gamma}t\right), & \tilde{\rho}(x, y) &= (1 + \delta T(x, y))^{1/(\gamma-1)}, \\ u_1(x, y, t) &= \tilde{u}_1\left(x - \frac{1}{\gamma}t, y - \frac{1}{\gamma}t\right), & \tilde{u}_1(x, y) &= \frac{1}{\gamma} + \delta u_1(x, y), \\ u_2(x, y, t) &= \tilde{u}_2\left(x - \frac{1}{\gamma}t, y - \frac{1}{\gamma}t\right), & \tilde{u}_2(x, y) &= \frac{1}{\gamma} + \delta u_2(x, y), \\ p(x, y, t) &= \tilde{p}\left(x - \frac{1}{\gamma}t, y - \frac{1}{\gamma}t\right), & \tilde{p}(x, y) &= (\tilde{\rho}(x, y))^\gamma. \end{aligned} \tag{34}$$

In Table 1, we present the errors and rates of convergence for  $N = 1, 2, 3$  and 4 using a modal DG formulation. The convergence rates are higher than the best  $L^2$  approximation convergence rates, but we anticipate that under further mesh refinement, these rates will decrease and approach  $N + 1$ . We note that similar errors and rates of convergence are obtained using both a BR-1 discretization of the artificial viscosity, as well as using a standard DG method with no artificial viscosity.

$K$	$L^2$ (N=1)	Order	$L^2$ (N=2)	Order
16	$3.134 \times 10^{-2}$	—	$7.770 \times 10^{-3}$	—
32	$1.201 \times 10^{-2}$	1.3834	$5.854 \times 10^{-4}$	3.7304
64	$2.290 \times 10^{-3}$	2.3914	$4.845 \times 10^{-5}$	3.5949
128	$3.522 \times 10^{-4}$	2.7006	$5.261 \times 10^{-6}$	3.2031
$K$	$L^2$ (N=3)	Order	$L^2$ (N=4)	Order
16	$1.274 \times 10^{-3}$	—	$3.567 \times 10^{-4}$	—
32	$8.356 \times 10^{-5}$	3.9308	$1.314 \times 10^{-5}$	4.7620
64	$4.201 \times 10^{-6}$	4.3141	$3.542 \times 10^{-7}$	5.2135
128	$2.176 \times 10^{-7}$	4.2706	$9.870 \times 10^{-9}$	5.1656

Table 1: Example 5.3: A h-refinement convergence table.  $2 \times K^2$  is the number of uniform triangular elements. The relative  $L_2$  error and approximate order of accuracy are also given for the corresponding values of  $K$ .

#### 5.4. Stationary Contact Wave and Contact Preservation

In the following stationary contact wave example, we demonstrate that ECAV is contact-preserving. Note that for piecewise constant initial conditions, the entropy correction artificial viscosity vanishes. The volume integral in the entropy residual (26) vanishes because  $\Pi_N \mathbf{v}_h$  is constant on each element. Similarly, since  $\psi_m(\bar{\mathbf{u}})$  is constant over each element, the boundary integral in the entropy residual reduces to the integral over  $\partial D^k$  of the outward normal component of a constant vector. Thus, if a baseline DG formulation is contact-preserving (e.g., if a contact preserving interface flux  $\mathbf{f}_n^*$  is used) then (16) is contact preserving.

To verify this, we consider the piecewise constant initial conditions

$$(\rho, u, p) = \begin{cases} (1.5, 0, 1) & |x| < 0.3 \\ (1, 0, 1) & |x| \geq 0.3, \end{cases} \quad (35)$$

and the piecewise smooth initial condition

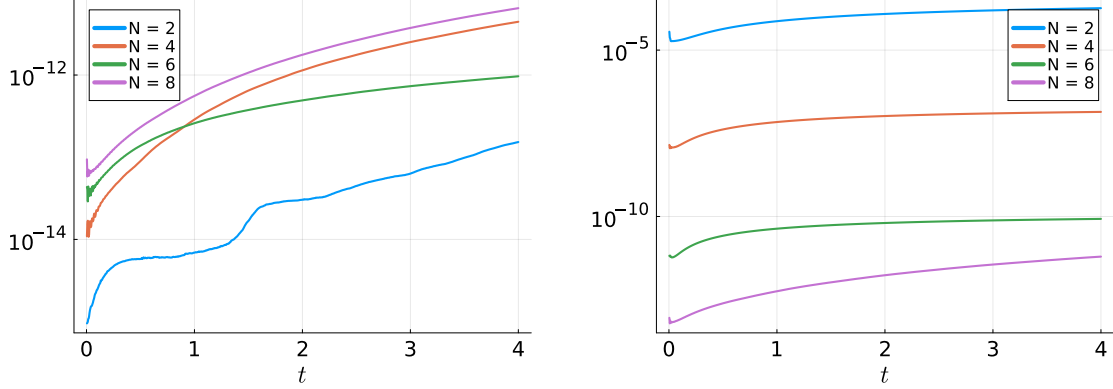
$$(\rho, u, p) = \begin{cases} (1 + 0.5(\sin(2\pi x) + |x|), 0, 1) & |x| < 0.3 \\ (1 + .5 \sin(2\pi x), 0, 1) & |x| \geq 0.3, \end{cases} \quad (36)$$

with a domain  $[-1.0, 1.0]$ , periodic boundary conditions, and a final time of  $t = 4.0$ . Since the piecewise constant initial conditions given by (35) are exactly representable by a DG basis, we expect to observe exact contact preservation in this case since the interface flux is the contact-preserving HLLC flux [7].

In Figure 2, we validate the contact preserving property of the proposed method by tracking the time evolution of the  $L^2$  error is plotted for  $N = 2, 4, 6, 8$ , a fixed time step of  $\Delta t = 5 \times 10^{-4}$ ,  $K = 80$  elements, for both initial conditions (35) and (36). With piecewise constant initial conditions, the stationary contact is preserved up to machine precision. For the piecewise smooth solution, the stationary contact is preserved over time up to high-order accuracy.

#### 5.5. Shock-vortex interaction

The next problem is the 2D shock-vortex interaction problem from [63]. We will examine how the entropy correction LDG artificial viscosity method resolves the interaction between the shock and the vortex. The domain is  $[0, 2] \times [0, 1]$  and a stationary Mach  $M_s = 1.1$  shock is



(a) Piecewise constant stationary solution (35)

(b) Piecewise smooth stationary solution (36)

Figure 2: Example 5.4, semi-log plots of the  $L^2$  error evolution for two different stationary contact solutions.

positioned at  $x = 0.5$  and normal to the x-axis. On the left of the shock the initial condition is  $(\rho_L, u_L, v_L, p_L) = (1, \sqrt{\gamma}, 0, 1)$ , and the initial conditions on the right side of the shock are computed using the Rankine-Hugoniot conditions

$$\frac{\rho_L}{\rho_R} = \frac{u_L}{u_R} = \frac{2 + (\gamma - 1)M_s^2}{(\gamma + 1)M_s^2}, \quad \frac{p_L}{p_R} = 1 + \frac{2\gamma}{\gamma + 1}(M_s^2 - 1), \quad v_R = 0.$$

An isentropic vortex is centered at  $(x_c, y_c) = (0.25, 0.5)$  is added as a perturbation of  $(u_1, u_2)$ , and temperature  $T = p/\rho$

$$\begin{aligned} \delta u_1 &= v_\theta \sin(\theta), & \delta u_2 &= -v_\theta \cos(\theta), \\ v_\theta &= \epsilon \tau \exp(\alpha(1 - \tau^2)), & \delta T &= -\frac{(\gamma - 1)\epsilon^2 \exp(2\alpha(1 - \tau^2))}{4\alpha\gamma} \end{aligned}$$

where  $r = \sqrt{(x - x_c)^2 + (y - y_c)^2}$ ,  $\tau = r/r_c$ ,  $\theta = \tan^{-1}(\frac{y - y_c}{x - x_c})$ ,  $\epsilon = 0.3$ ,  $\alpha = 0.204$ , and  $r_c = 0.05$ . Finally, entropy  $S = \ln(p/\rho^\gamma)$  is not perturbed and our initial conditions are

$$(\rho, u_1, u_2, p) = \begin{cases} \left( \rho_L \left( \frac{T_L + \delta T}{T_L} \right)^{\frac{1}{\gamma-1}}, u_L + \delta u_1, v_L + \delta u_2, p_L \left( \frac{T_L + \delta T}{T_L} \right)^{\frac{1}{\gamma-1}} \right) & x < 0.5 \\ \left( \rho_R \left( \frac{T_L + \delta T}{T_L} \right)^{\frac{1}{\gamma-1}}, u_R + \delta u_1, v_R + \delta u_2, p_R \left( \frac{T_L + \delta T}{T_L} \right)^{\frac{1}{\gamma-1}} \right) & x > 0.5 \end{cases}$$

We will enforce the same boundary conditions as [15], periodic boundary conditions on the left and right boundaries, and wall boundary conditions on the top and bottom boundaries. Using a  $128 \times 64$  element mesh and  $N = 2$ , in Figure 3 we plot the density profile and the numerical Schlieren data at times  $t = 0$ ,  $t = 0.2$  and  $t = 0.7$ . The numerical Schlieren plot visualizes gradients of the density field by plotting the quantity:

$$\rho^{schl} = \exp\left(-10 \frac{g - g_{\min}}{g_{\max} - g_{\min}}\right), \quad g = \|\nabla \rho\|, \quad g_{\min} = \min_{x \in D} g(x), \quad g_{\max} = \max_{x \in D} g(x). \quad (37)$$

In the numerical Schlieren plots, we observe that while oscillations are present, they remain localized around the vicinity of the shock.

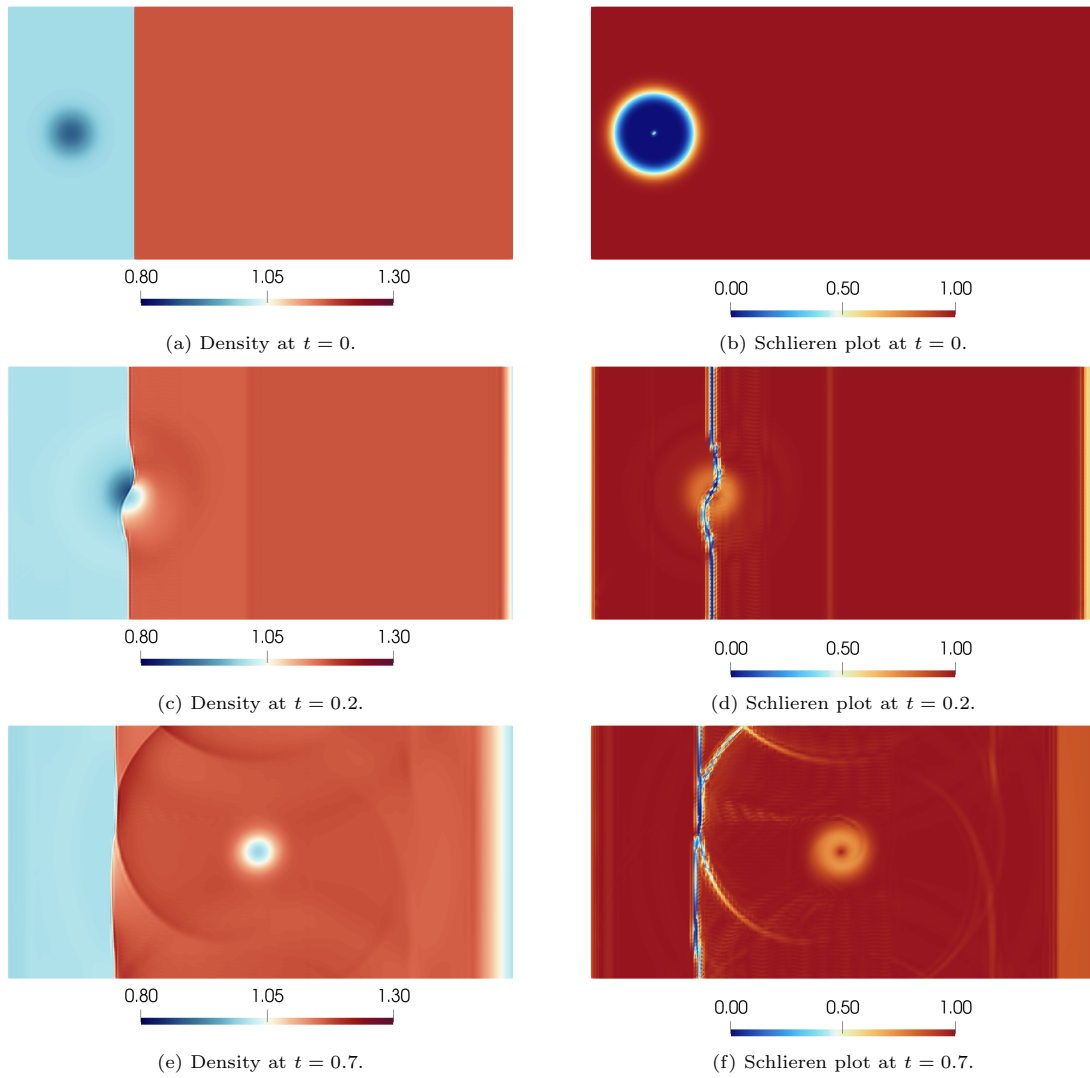


Figure 3: Example 5.7, density profiles and numerical Schlieren plots.

### 5.6. 1D Density Wave

In the following example we compare the proposed ECAV method to a high order shock capturing method [55]. The shock capturing method utilizes the smoothness indicator on element  $D^k$  introduced in [39]

$$S_k = \max\left(\tilde{S}_k^N, \tilde{S}_k^{N-1}\right), \quad (38)$$

where  $\tilde{S}_k^N$  is given by

$$\tilde{S}_k^N = \frac{(u_h - \hat{u}_h, u_h - \hat{u}_h)_{D^k}}{(u_h, u_h)_{D^k}}, \quad u_h = \sum_{j=1}^N u_j \psi_j, \quad \hat{u}_h = \sum_{j=1}^{N-1} u_j \psi_j, \quad (39)$$

and  $u_h$  and  $\hat{u}_h$  are the indicator variables expressed in terms of the orthogonal basis  $\{\psi_j\}_{j=1}^N$ . In [39] the indicator variables  $u$  are chosen as the product of the density and pressure variables.

For continuous solutions in one dimension, the  $j^{\text{th}}$  Fourier coefficient scales as  $\sim 1/j^2$ ; therefore we expect that  $S_k \sim 1/N^4$ . This behavior is also expected for a general modal polynomial basis [47]. Intuitively, artificial viscosity should be added if  $S_k > 1/N^4$ , and is thus defined based on the following formula:

$$\epsilon_k(s_k) = \begin{cases} 0 & \text{if } s_k < s_0 - \kappa \\ \frac{\epsilon_0}{2} \left(1 + \sin \frac{\pi(s_k - s_0)}{2\kappa}\right) & \text{if } s_0 - \kappa \leq s_k \leq s_0 + \kappa \\ \epsilon_0 & \text{if } s_k > s_0 + \kappa, \end{cases} \quad (40)$$

where  $s_k = \log_{10} S_k$  and the parameters  $\epsilon_0 \sim h/N$ ,  $s_0 \sim \log_{10}(1/N^4)$ , and  $\kappa$  are chosen empirically so that a sharp but smooth shock profile is obtained. In the following numerical example, we use  $s_0$  and  $\kappa$  that are provided in [69], where  $s_0 + \kappa = -4 \log_{10} N$  and  $s_0 - \kappa = -11 \log_{10} N$ . We choose  $\epsilon_0 = h/(2N)$ ; however, other values such as  $\epsilon_0 = 3h/(2N)$  and  $\epsilon_0 = 9h/(2N)$  resulted in similar behavior.

We consider the 1D density wave problem with initial conditions:

$$\rho = 1.0 + 0.5 \exp\left(-10 \sin(\pi x)^2\right), \quad u = 0.1, \quad p = 10.0, \quad (41)$$

with periodic boundary conditions. The solution to the density wave problem is approximated from  $t = 0$  to a final time of  $t = 25$  using the entropy correction artificial viscosity (ECAV) method and the shock capturing (SC) method. For both methods, we use degree  $N = 5$  polynomials.

Figure 4 shows the time evolution of the maximum artificial viscosity coefficient and Figure 5 shows the time evolution of the  $L^2$  error for the shock capturing and entropy correction artificial viscosity methods using  $K = 8$  and  $K = 16$  elements. In Figure 6, the density profile at the final time for the ECAV and shock capturing method is compared to the exact solution at the final time. At these resolutions, we observe that the entropy correction artificial viscosity method generally results in a smaller maximum artificial viscosity and a smaller  $L^2$  error than the shock capturing method.

In Table 2, we additionally compare  $L^2$  errors of the ECAV and the DG method with no added viscosity at the final time  $t = 25$ . We observe that the error of the ECAV solution is larger than the  $L^2$  norm of the difference between the ECAV solution and standard DG solution. The similarity of the two solutions is expected in this situation where we have a smooth solution and the ECAV method adds a minimal amount of artificial viscosity.

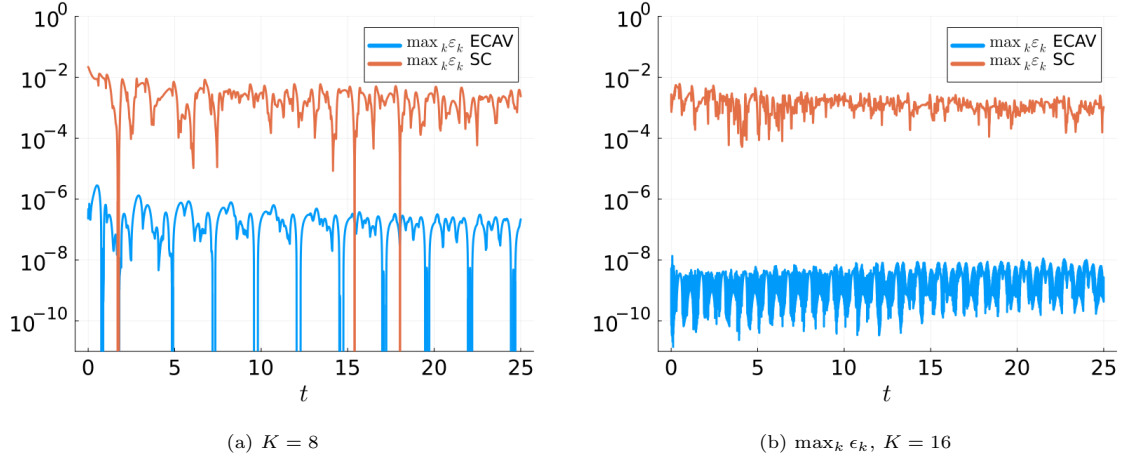


Figure 4: Example 5.6, time evolution of the  $\max_k \epsilon_k$  (semi-log plot) using shock capturing (labeled “SC”) and entropy correction artificial viscosity (labeled “ECAV”) for degree  $N = 5$  and both  $K = 8$  and  $K = 16$  elements.

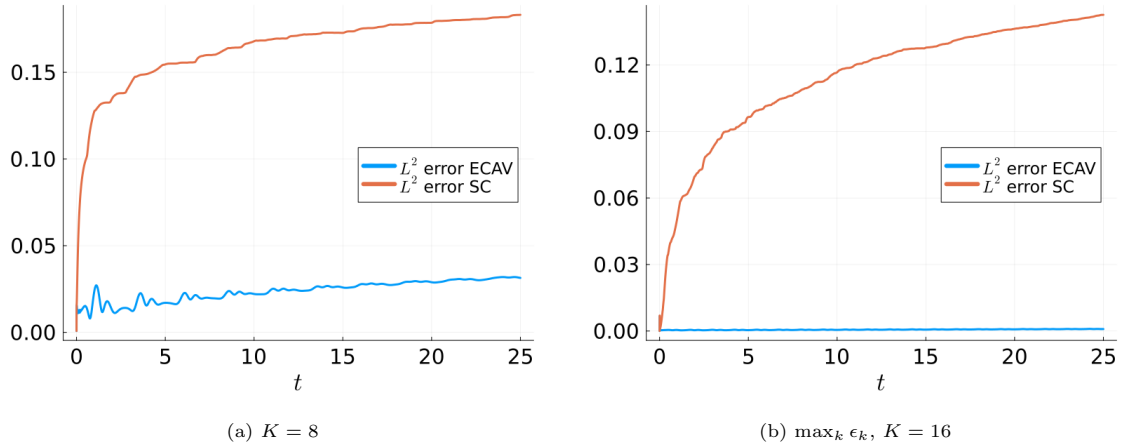


Figure 5: Example 5.6, time evolution of the  $L^2$  error using shock capturing (labeled “SC”) and entropy correction artificial viscosity (labeled “ECAV”) for degree  $N = 5$  and both  $K = 8$  and  $K = 16$  elements.

$K$	$L^2$ error $\mathbf{u}_{\text{ECAV}}$	$L^2$ error $\mathbf{u}_{\text{DG}}$	$L^2$ norm of $\mathbf{u}_{\text{ECAV}} - \mathbf{u}_{\text{DG}}$
8	$3.142 \times 10^{-2}$	$3.140 \times 10^{-2}$	$6.979 \times 10^{-5}$
16	$8.835 \times 10^{-4}$	$8.831 \times 10^{-4}$	$2.690 \times 10^{-5}$
24	$7.503 \times 10^{-5}$	$7.438 \times 10^{-5}$	$9.754 \times 10^{-6}$

Table 2: Example 5.6: A table comparing the errors of the ECAV solution and the DG (no added viscosity) solution and the  $L^2$  norm of the difference between the two methods at the final time  $t = 25$ .

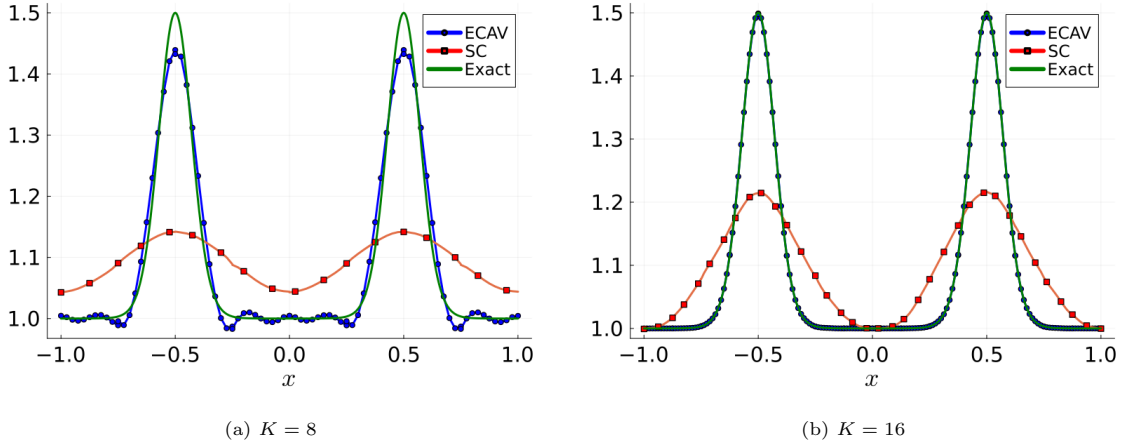


Figure 6: Example 5.6, Density profile at the final time  $t = 25.0$  for the exact solution (labeled “Exact”), the shock capturing (labeled “SC”), and the entropy correction artificial Viscosity (labeled “ECAV”) using  $K = 8$  and  $K = 16$  elements.

### 5.7. Shu-Osher problem

This example problem is the Shu-Osher sine-shock interaction problem from [64] with initial conditions

$$(\rho, u, p) = \begin{cases} (3.857143, 2.629369, 10.3333) & x < -4 \\ (1 + 0.2 \sin(5x), 0, 1) & x \geq -4, \end{cases}$$

on the domain  $[-5, 5]$  and a final time of  $t = 1.8$ . We use  $K = 100$  elements and polynomials of degree  $N = 3$ . Figure 7a is a plot of the time evolution of the quantity  $\|\delta\mathbf{v}\|_{L^2(D^k)}^2 / \|\Pi_N \delta\mathbf{v}\|_{L^2(D^k)}^2$  from Lemma 4 and we see that it remains close to one with a modal LDG formulation. In Figure 7, we can observe that the density profiles for local DG and BR-1 discretizations of ECAV are similar.

Interestingly, when using modal DG, the number of adaptive time steps when using LDG is 4218 compared to 7483 when using BR-1, although the maximum  $\epsilon_k$  is often slightly larger for LDG. When using a nodal DG discretization (e.g., a discontinuous Galerkin spectral element discretization with  $(N + 1)$ -point Legendre-Gauss-Lobatto quadrature, which results in a diagonal mass matrix and collocation-like scheme), the number of time steps is roughly the same, 4063 for LDG and 4116 for BR-1.

In Figure 8, we compare the time evolution of the maximum value of  $\epsilon_k$  for BR-1 and local DG with both modal and nodal DG formulations. Because the maximum values of  $\epsilon_k$  over time are similar for both LDG and BR-1, this suggests that the magnitude of the ECAV coefficient is not responsible for the increased number of time-steps under a BR-1 discretization.

We explored other possible explanations for this behavior, such as comparing  $\|\sigma\|_{L^2(\omega)}$  from (18) or comparing the norm of the ODE right-hand side over time. In all examples, we did not observe significant differences between LDG and BR-1. Because the difference in the number of time-steps is observed only for the modal formulation, we conjecture that the projection of the entropy variables is a factor. However, other differences between LDG and BR-1 [3] could also be a factor.

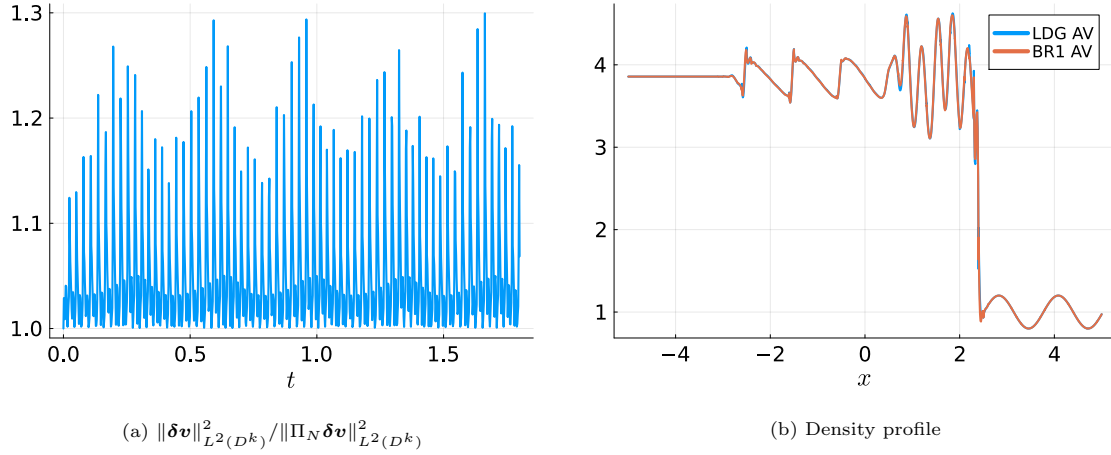


Figure 7: Example 5.7, Time evolution of  $\|\delta v\|_{L^2(D^k)}^2 / \|\Pi_N \delta v\|_{L^2(D^k)}^2$  from Lemma 4 and density profile at the final time  $t = 1.8$  for both the LDG and BR-1 EVAC discretizations with a modal formulation.

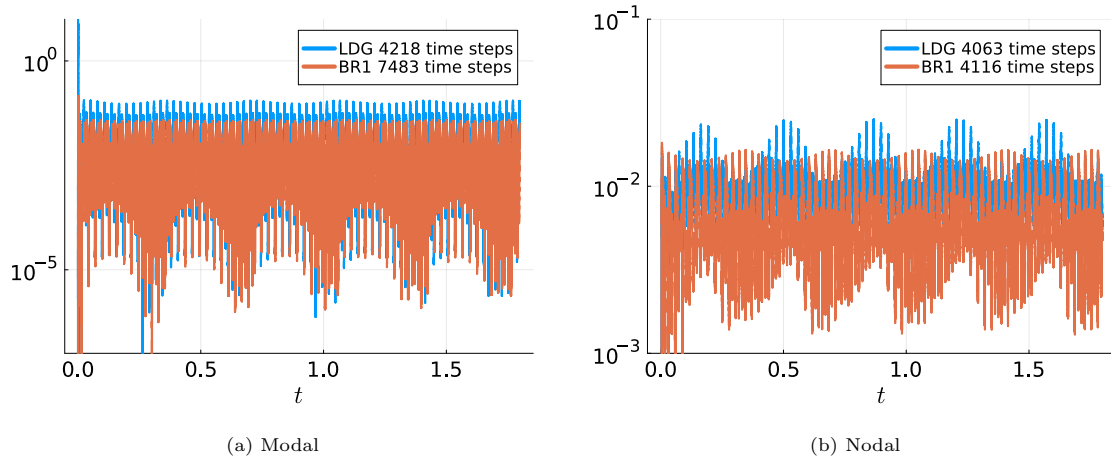


Figure 8: Example 5.7, Time evolution of the  $\max_k \epsilon_k$  (semi-log plot) for modal and nodal formulations.

## 6. Conclusions

In this paper, we analyze the behavior of entropy correction artificial viscosity (ECAV) [14] under a local DG viscous discretization. We prove that, unlike BR-1 viscous discretizations, the norm of the DG gradients are bounded below, resulting in an  $O(h)$  upper bound on the artificial viscosity coefficient. Additionally, we show that the resulting local DG viscous discretization satisfies the same entropy inequality derived in [14] and is contact preserving.

Numerical experiments show that it is possible for the ECAV coefficient produced by the BR-1 viscous discretization to become arbitrarily large, resulting in a much smaller maximum stable time-step. We also compare against a more standard modal shock capturing method to illustrate that ECAV is minimally dissipative. Finally, we validate the high-order accuracy and entropy stability of the proposed method.

## 7. Acknowledgements

The authors thank Keegan Kirk and Hendrik Ranocha for helpful discussions. Jesse Chan gratefully acknowledges support from National Science Foundation (NSF) under award DMS-1943186. Samuel Van Fleet acknowledges support from the NSF under award DMS-223148.

## References

- [1] Remi Abgrall. A general framework to construct schemes satisfying additional conservation relations. Application to entropy conservative and entropy dissipative schemes. *Journal of Computational Physics*, 372:640–666, 2018.
- [2] Rémi Abgrall, Philipp Öffner, and Hendrik Ranocha. Reinterpretation and extension of entropy correction terms for residual distribution and discontinuous Galerkin schemes: application to structure preserving discretization. *Journal of Computational Physics*, 453:110955, 2022.
- [3] Mohammad A Alhawwary and Zhi J Wang. A study of DG methods for diffusion using the combined-mode analysis. In *AIAA Scitech 2019 Forum*, page 1157, 2019.
- [4] Boris D Andrews and Patrick E Farrell. High-order conservative and accurately dissipative numerical integrators via auxiliary variables. *arXiv preprint arXiv:2407.11904*, 2024.
- [5] Douglas N Arnold, Franco Brezzi, Bernardo Cockburn, and L Donatella Marini. Unified analysis of discontinuous Galerkin methods for elliptic problems. *SIAM journal on numerical analysis*, 39(5):1749–1779, 2002.
- [6] Timothy J Barth. Numerical methods for gasdynamic systems on unstructured meshes. In *An Introduction to Recent Developments in Theory and Numerics for Conservation Laws*, pages 195–285. Springer, 1999.
- [7] Paul Batten, Nicholas Clarke, Claire Lambert, and Derek M Causon. On the choice of wavespeeds for the HLLC Riemann solver. *SIAM Journal on Scientific Computing*, 18(6):1553–1570, 1997.

- [8] Christophe Berthon, Manuel J Castro Díaz, Arnaud Duran, Tomás Morales de Luna, and Khaled Saleh. Artificial viscosity to get both robustness and discrete entropy inequalities. *Journal of Scientific Computing*, 97(3):65, 2023.
- [9] Marvin Bohm, Andrew R. Winters, Gregor J. Gassner, Dominik Derigs, Florian Hindenlang, and Joachim Saur. An entropy stable nodal discontinuous Galerkin method for the resistive MHD equations. Part I: Theory and numerical verification. *Journal of Computational Physics*, 422:108076, 2020.
- [10] Susanne C Brenner. Poincaré–Friedrichs Inequalities for Piecewise  $H^1$  Functions. *SIAM Journal on Numerical Analysis*, 41(1):306–324, 2003.
- [11] Mark H Carpenter, Travis C Fisher, Eric J Nielsen, and Steven H Frankel. Entropy stable spectral collocation schemes for the Navier-Stokes equations: Discontinuous interfaces. *SIAM Journal on Scientific Computing*, 36(5):B835–B867, 2014.
- [12] Carsten Carstensen and Friederike Hellwig. Constants in discrete Poincaré and Friedrichs inequalities and discrete quasi-interpolation. *Computational Methods in Applied Mathematics*, 18(3):433–450, 2018.
- [13] Jesse Chan. On discretely entropy conservative and entropy stable discontinuous Galerkin methods. *Journal of Computational Physics*, 362:346–374, 2018.
- [14] Jesse Chan. An artificial viscosity approach to high order entropy stable discontinuous Galerkin methods. *Journal of Computational Physics*, 543:114380, 2025.
- [15] Jesse Chan, David C Del Rey Fernandez, and Mark H Carpenter. Efficient entropy stable Gauss collocation methods. *SIAM Journal on Scientific Computing*, 41(5):A2938–A2966, 2019.
- [16] Jesse Chan, Yimin Lin, and Tim Warburton. Entropy stable modal discontinuous Galerkin schemes and wall boundary conditions for the compressible Navier-Stokes equations. *Journal of Computational Physics*, 448:110723, 2022.
- [17] Jesse Chan, Hendrik Ranocha, Andrés M Rueda-Ramírez, Gregor Gassner, and Tim Warburton. On the entropy projection and the robustness of high order entropy stable discontinuous Galerkin schemes for under-resolved flows. *Frontiers in Physics*, 10:898028, 2022.
- [18] Praveen Chandrashekar. Kinetic energy preserving and entropy stable finite volume schemes for compressible Euler and Navier-Stokes equations. *Communications in Computational Physics*, 14(5):1252–1286, 2013.
- [19] Tianheng Chen and Chi-Wang Shu. Entropy stable high order discontinuous Galerkin methods with suitable quadrature rules for hyperbolic conservation laws. *Journal of Computational Physics*, 345:427–461, 2017.
- [20] Brian Christner and Jesse Chan. Entropy stable finite difference methods via entropy correction artificial viscosity and knapsack limiting. *arXiv preprint arXiv:2508.21226*, 2025.
- [21] Brian Christner and Jesse Chan. Entropy Stable Nodal Discontinuous Galerkin Methods via Quadratic Knapsack Limiting. *arXiv preprint arXiv:2507.14488*, 2025.

- [22] Alexander Cicchino and Siva Nadarajah. Discretely nonlinearly stable weight-adjusted flux reconstruction high-order method for compressible flows on curvilinear grids. *Journal of Computational Physics*, 521:113532, 2025.
- [23] Bernardo Cockburn and Bo Dong. An analysis of the minimal dissipation local discontinuous Galerkin method for convection–diffusion problems. *Journal of Scientific Computing*, 32:233–262, 2007.
- [24] Bernardo Cockburn, Guido Kanschat, Ilaria Perugia, and Dominik Schötzau. Superconvergence of the local discontinuous Galerkin method for elliptic problems on Cartesian grids. *SIAM Journal on Numerical Analysis*, 39(1):264–285, 2001.
- [25] Bernardo Cockburn and Chi-Wang Shu. The local discontinuous Galerkin method for time-dependent convection-diffusion systems. *SIAM journal on numerical analysis*, 35(6):2440–2463, 1998.
- [26] Alessandra Colombo, Andrea Crivellini, and Alessandra Nigro. On the entropy conserving/stable implicit DG discretization of the Euler equations in entropy variables. *Computers & Fluids*, 232:105198, 2022.
- [27] Constantine M Dafermos. *Hyperbolic conservation laws in continuum physics*, volume 3. Springer, 2005.
- [28] Ayaboe K Edoh. Conservative correction procedures utilizing artificial dissipation operators. *Journal of Computational Physics*, 504:112880, 2024.
- [29] Imre Fekete, Sidafa Conde, and John N. Shadid. Embedded pairs for optimal explicit strong stability preserving Runge–Kutta methods. *Journal of Computational and Applied Mathematics*, 412:114325, 2022.
- [30] David Flad and Gregor Gassner. On the use of kinetic energy preserving DG-schemes for large eddy simulation. *Journal of Computational Physics*, 350:782–795, 2017.
- [31] K. O. Friedrichs and P. D. Lax. Systems of Conservation Equations with a Convex Extension. *Proceedings of the National Academy of Sciences*, 68:1686–1688, 1971.
- [32] Elena Gaburro, Philipp Öffner, Mario Ricchiuto, and Davide Torlo. High order entropy preserving ADER-DG schemes. *Applied Mathematics and Computation*, 440:127644, 2023.
- [33] Gregor J Gassner. A skew-symmetric discontinuous Galerkin spectral element discretization and its relation to SBP-SAT finite difference methods. *SIAM Journal on Scientific Computing*, 35(3):A1233–A1253, 2013.
- [34] Gregor J Gassner, Andrew R Winters, and David A Kopriva. Split form nodal discontinuous Galerkin schemes with summation-by-parts property for the compressible Euler equations. *Journal of Computational Physics*, 327:39–66, 2016.
- [35] Ioannis Gkanis and Charalambos Makridakis. A new class of entropy stable schemes for hyperbolic systems: Finite element methods. *Mathematics of Computation*, 90(330):1663–1699, 2021.

- [36] Jan Glaubitz, AC Nogueira, João LS Almeida, RF Cantão, and CAC Silva. Smooth and compactly supported viscous sub-cell shock capturing for discontinuous Galerkin methods. *Journal of Scientific Computing*, 79:249–272, 2019.
- [37] Edwige Godlewski and Pierre-Arnaud Raviart. *Numerical approximation of hyperbolic systems of conservation laws*, volume 118. Springer Science & Business Media, 2013.
- [38] Jean-Luc Guermond, Richard Pasquetti, and Bojan Popov. Entropy viscosity method for nonlinear conservation laws. *Journal of Computational Physics*, 230(11):4248–4267, 2011.
- [39] Sebastian Hennemann, Andrés M Rueda-Ramírez, Florian J Hindenlang, and Gregor J Gassner. A provably entropy stable subcell shock capturing approach for high order split form DG for the compressible Euler equations. *Journal of Computational Physics*, 426:109935, 2021.
- [40] Jan S Hesthaven and Tim Warburton. *Nodal discontinuous Galerkin methods: algorithms, analysis, and applications*. Springer Science & Business Media, 2007.
- [41] Jason E Hicken, David C Del Rey Fernández, and David W Zingg. Multidimensional summation-by-parts operators: general theory and application to simplex elements. *SIAM Journal on Scientific Computing*, 38(4):A1935–A1958, 2016.
- [42] Farzad Ismail and Philip L Roe. Affordable, entropy-consistent Euler flux functions II: Entropy production at shocks. *Journal of Computational Physics*, 228(15):5410–5436, 2009.
- [43] Guang Shan Jiang and Chi-Wang Shu. On a cell entropy inequality for discontinuous Galerkin methods. *Mathematics of Computation*, 62(206):531–538, 1994.
- [44] Lorenz John, Michael Neilan, and Iain Smears. Stable discontinuous Galerkin FEM without penalty parameters. In *Numerical mathematics and advanced applications ENUMATH 2015*, pages 165–173. Springer, 2016.
- [45] George Karniadakis and Spencer J Sherwin. *Spectral/hp element methods for computational fluid dynamics*. Oxford University Press, USA, 2005.
- [46] Jens Keim, Anna Schwarz, Patrick Kopper, Marcel Blind, Christian Rohde, and Andrea Beck. Entropy stable high-order discontinuous Galerkin spectral-element methods on curvilinear, hybrid meshes. *arXiv preprint arXiv:2507.04334*, 2025.
- [47] Andreas Klöckner, Tim Warburton, and Jan S Hesthaven. Viscous shock capturing in a time-explicit discontinuous Galerkin method. *Mathematical Modelling of Natural Phenomena*, 6(3):57–83, 2011.
- [48] Johannes Franciscus Bernardus Maria Kraaijevanger. Contractivity of Runge-Kutta methods. *BIT Numerical Mathematics*, 31(3):482–528, 1991.
- [49] Yu Lv, Yee Chee See, and Matthias Ihme. An entropy-residual shock detector for solving conservation laws using high-order discontinuous Galerkin methods. *Journal of Computational Physics*, 322:448–472, 2016.
- [50] Andrew Majda and Stanley Osher. Numerical viscosity and the entropy condition. *Communications on Pure and Applied Mathematics*, 32(6):797–838, 1979.

- [51] Yogiraj Mantri, Philipp Öffner, and Mario Ricchiuto. Fully well-balanced entropy controlled discontinuous Galerkin spectral element method for shallow water flows: global flux quadrature and cell entropy correction. *Journal of Computational Physics*, 498:112673, 2024.
- [52] Georgii Oblapenko and Manuel Torrilhon. Entropy-conservative high-order methods for high-enthalpy gas flows. *Computers and Fluids*, 295:106640, 2025.
- [53] Matteo Parsani, Radouan Boukharfane, Irving Reyna Nolasco, David C. Del Rey Fernández, Stefano Zampini, Bilel Hadri, and Lisandro Dalcin. High-order accurate entropy-stable discontinuous collocated Galerkin methods with the summation-by-parts property for compressible CFD frameworks: Scalable SSDC algorithms and flow solver. *Journal of Computational Physics*, 424:109844, 2021.
- [54] P-O Persson. The compact discontinuous Galerkin (CDG) method for elliptic problems. *SIAM Journal on Scientific Computing*, 30(4):1806–1824, 2008.
- [55] Per-Olof Persson and Jaime Peraire. Sub-cell shock capturing for discontinuous Galerkin methods. In *44th AIAA Aerospace Sciences Meeting and Exhibit*, page 112, 2006.
- [56] Ahmad Peyvan, Khemraj Shukla, Jesse Chan, and George Karniadakis. High-order methods for hypersonic flows with strong shocks and real chemistry. *Journal of Computational Physics*, 490:112310, 2023.
- [57] Christopher Rackauckas and Qing Nie. Differentialequations. jl—a performant and feature-rich ecosystem for solving differential equations in Julia. *Journal of open research software*, 5(1):15–15, 2017.
- [58] Hendrik Ranocha. Comparison of some entropy conservative numerical fluxes for the Euler equations. *Journal of Scientific Computing*, 76(1):216–242, 2018.
- [59] Hendrik Ranocha, Lisandro Dalcin, Matteo Parsani, and David I Ketcheson. Optimized Runge-Kutta methods with automatic step size control for compressible computational fluid dynamics. *Communications on Applied Mathematics and Computation*, 4(4):1191–1228, 2022.
- [60] Hendrik Ranocha, Michael Schlottke-Lakemper, Andrew R Winters, Erik Faulhaber, Jesse Chan, and Gregor J Gassner. Adaptive numerical simulations with Trixi.jl: A case study of Julia for scientific computing. In *Proceedings of the JuliaCon Conferences*, volume 1, page 77, 2022.
- [61] Andrés M. Rueda-Ramírez, Sebastian Hennemann, Florian J. Hindenlang, Andrew R. Winters, and Gregor J. Gassner. An entropy stable nodal discontinuous Galerkin method for the resistive MHD equations. Part II: Subcell finite volume shock capturing. *Journal of Computational Physics*, 444:110580, 2021.
- [62] SJ Sherwin, RM Kirby, J Peiró, RL Taylor, and OC Zienkiewicz. On 2D elliptic discontinuous Galerkin methods. *International journal for numerical methods in engineering*, 65(5):752–784, 2006.
- [63] Chi-Wang Shu. Essentially non-oscillatory and weighted essentially non-oscillatory schemes for hyperbolic conservation laws. In Alfio Quarteroni, editor, *Advanced Numerical Approximation of Nonlinear Hyperbolic Equations*, pages 325–432. Springer Berlin Heidelberg, Berlin, Heidelberg, 1998.

- [64] Chi-Wang Shu. High order weighted essentially nonoscillatory schemes for convection dominated problems. *SIAM review*, 51(1):82–126, 2009.
- [65] Seth C. Spiegel, H. T. Huynh, and James R. DeBonis. A Survey of the Isentropic Euler Vortex Problem using High-Order Methods. In *22nd AIAA Computational Fluid Dynamics Conference*, Dallas, TX, 2015. American Institute of Aeronautics and Astronautics. AIAA Paper 2015-2444.
- [66] Eitan Tadmor. The numerical viscosity of entropy stable schemes for systems of conservation laws. I. *Mathematics of Computation*, 49(179):91–103, 1987.
- [67] Eitan Tadmor. Entropy stability theory for difference approximations of nonlinear conservation laws and related time-dependent problems. *Acta Numerica*, 12(1):451–512, 2003.
- [68] Ch. Tsitouras. Runge–Kutta pairs of order 5(4) satisfying only the first column simplifying assumption. *Computers and Mathematics with Applications*, 62(2):770–775, 2011.
- [69] Jordi Vila-Pérez, Matteo Giacomini, Ruben Sevilla, and Antonio Huerta. Hybridisable Discontinuous Galerkin Formulation of Compressible Flows. *Archives of Computational Methods in Engineering*, 28(2):753–784, 2021.
- [70] John VonNeumann and Robert D Richtmyer. A method for the numerical calculation of hydrodynamic shocks. *Journal of applied physics*, 21(3):232–237, 1950.
- [71] David M Williams. An analysis of discontinuous Galerkin methods for the compressible Euler equations: entropy and  $L^2$  stability. *Numerische Mathematik*, 141(4):1079–1120, 2019.
- [72] Niklas Wintermeyer, Andrew R Winters, Gregor J Gassner, and David A Kopriva. An entropy stable nodal discontinuous Galerkin method for the two dimensional shallow water equations on unstructured curvilinear meshes with discontinuous bathymetry. *Journal of Computational Physics*, 340:200–242, 2017.
- [73] Niklas Wintermeyer, Andrew R Winters, Gregor J Gassner, and Timothy Warburton. An entropy stable discontinuous Galerkin method for the shallow water equations on curvilinear meshes with wet/dry fronts accelerated by GPUs. *Journal of Computational Physics*, 375:447–480, 2018.